

Before I respond all the comments, I want to show my gratitude to the reviewers. It is my honor to get this constructive comments and suggestions. The reviewer not only pointed out the shortcoming of the paper, but also provided suggestions for revisions, and even recommended several excellent papers to me. I really learned a lot from this comment with comprehensive thinking, precise logic, and excellent formatting. This is a very important paper for us , we really take every piece of valuable comment very seriously, we adopted all the constructive suggestions and responded all the comments as followings. In addition, I will keep this document all the time to inspire myself in my whole academic career. And we really want to show our gratitude to reviewers with the real name in the acknowledgement , please contact us if it is possible.

10

Yu Tian (On behalf of all authors)

Email:tybgys455429145@163.com

15 *General Comments*

• Terminology

1. The paper denotes the gravity anomaly/gradient data sets that were reduced for multiple effects as "remaining" gravity anomaly/gradient. Using a term that is commonly used in gravimetry would be more appropriate (e.g., "corrected" for the effect of " etc.)

Response: We have used the term "corrected" to replace the term "remaining" throughout the whole paper.

25

2. Throughout the paper: "resultant data" → "resulting data"?

Response: We have used the term "resulting" to replace the term "resultant" throughout the whole paper.

3. Based on the paper that two referees recommended, we have used the term "terrestrial" to replace the term "surface" ; based on the inversion classification, we have used the term "sequential inversion" to replace the term "joint inversion" ; we have changed the title to " Sequential inversion of GOCE satellite gravity gradient data and terrestrial gravity data for the lithospheric density structure in the North China Craton".

35

• Formatting

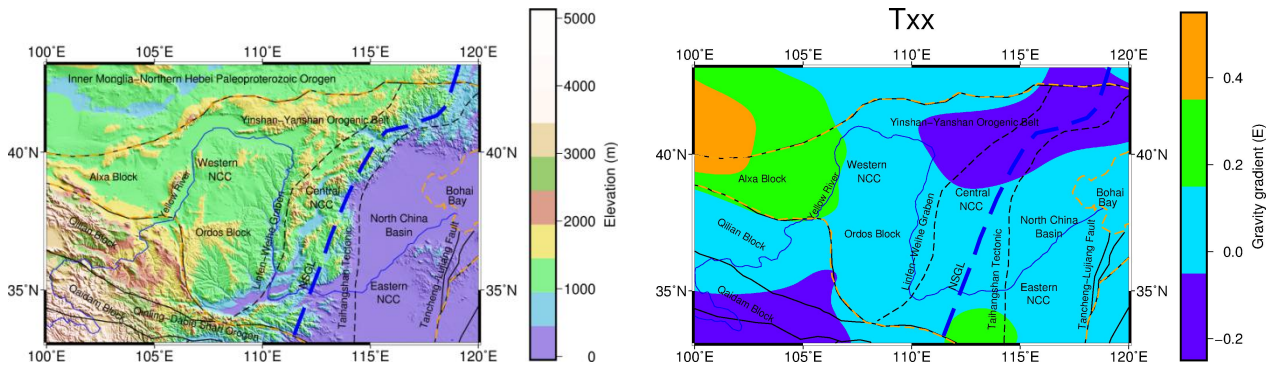
In the text, white spacing is often missing when Figures are mentioned, look for ”...(Fig...)”

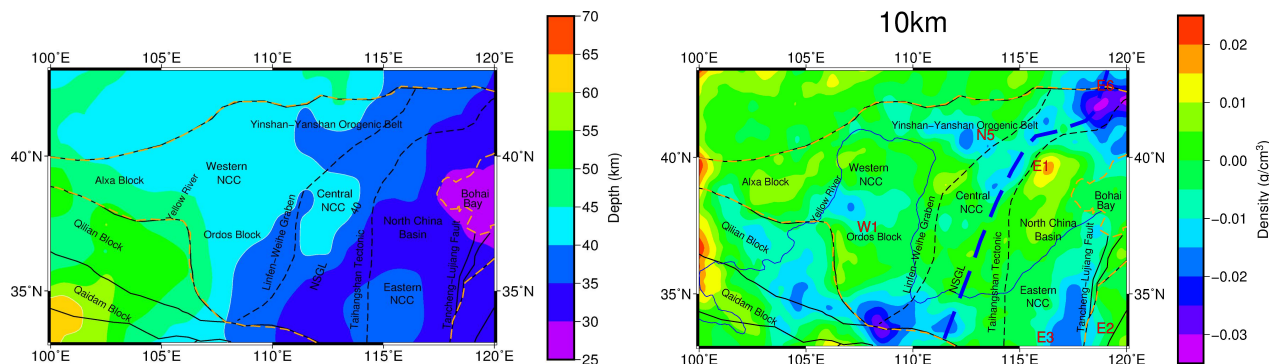
- 40 **Response:** We have already checked the white spacing between the bracket “()” and the term ”Fig”; and the white spacing between the term “Fig” and the following numbers.

• Figures

- 45 **4. Figures - on the top of the colorbars is a slash followed with a unit (probably coming from the panels with densities). Can it be removed (it is confusing)?**

Response: We have removed the unit on the top of colorbars and presented the unit (elevation, depth, gravity gradient, density) along with the colorbars as followings. We have updated all the figures throughout the paper.





55 5. **IMPORTANT:** Figures 2,3 have different colorbars for the input and the output. Please, update them to have the same colorbar span.

Response: (Page 11 and Page 12)

We have updated five figures in Figures 2 with the same colorbar (0.2g/cm^3 - 1.0g/cm^3), we have updated
60 five figures in Figures 3 with the same colorbar (0.1g/cm^3 - 1.0g/cm^3) in the paper .

Detailed comments (We have carefully followed all the comments on words, sentences, grammar, we have marked in red throughout the revised submission. The order is important questions throughout the paper first, then the detailed questions.)

65

Important questions

• 1. (1) 167 Reformulate the sentence and see Martinec, Z. (2014). Mass-density Green's functions for the gravitational gradient tensor at different heights. *Geophysical Journal International*,
70 196(3), 1455-1465. ... not all gradients have the kernel with the properties as you describe (what you describe is related to the radial derivatives)

(2) 176 **IMPORTANT.** You use some damping function to revert the kernel behaviour. Why do you use the same for all the gradients if their kernels behave differently?

Response:

75 This is a very important part that we did not describe in detail. The kernel functions are calculated under the Cartesian coordinate instead of the spherical coordinate, therefore we added the whole section " 2.1 Kernel function calculation" in Section 2. We have provided the detailed integral and analytical equations, which have the properties as we described in the depth weighting function. And for better understanding, we added the description about the kernel function after the Equation (6). In fact,

80 we used the different kernel functions corresponding to each gravity gradient components, we have provided the detailed description in the revised version.

The recommended paper (Martinec Z., 2014) presents the kernel function calculated in spherical coordinate, this is a very good paper which describes the advantage and disadvantage of the gravitational gradient tensor at different heights, we have cited this paper in the section "3.2 Downward Continuation".

Revision: (Page 5)

1. We have added section "2.1 Kernel function calculation".

90 **(Page 6)**

2. The description about the kernel function after the Equation (6) when we first mentioned the Kernel function in "Section 2.2 Inversion method".

"for gravity data, $G = G_z$, while for gravity gradient components, $G = [G_{xx}, G_{xz}, G_{yy}, G_{zz}]^T$ ".

95

• 2. (1) **Table 1 IMPORTANT. Could you add the real densities used in the model. The table gives just the initial values but not true ones so the reader cannot compare the result with the truth.**

(2) **266 You claim "that is almost identical to the true model". If I have not overlooked something, I did not find the true values so the claim cannot be checked by the reader. As said above, updating Table 1 with true values would help. Note "almost identical" is soft characteristics - it is more convenient to use RMS or so.**

Response: We have added the real densities of the true model, and RMS in both Table 1 and Table 2 as following.

105

Revision: (Page 10)

Table 1 Conditions and results for initial density model one.

| | True density at each layer (g/cm ³) (1 st to 4 th layer) | Initial density at each layer (g/cm ³) (1 st to 4 th layer) | Iterations (k) | RMS (E) | Maximum density at each layer (g/cm ³) (1 st to 4 th layer) |
|--------|---|--|-------------------|------------------------|--|
| Test 1 | (0.4, 0.7, 0.7, 1.0) | (0, 0, 0, 0) | 10 | 7.35×10 ⁻¹¹ | (0.34, 0.42, 0.53, 0.55) |
| Test 2 | (0.4, 0.7, 0.7, 1.0) | (0.4, 0.4, 0.4, 0.4) | 7 | 6.94×10 ⁻¹² | (0.51, 0.55, 0.66, 0.58) |
| Test 3 | (0.4, 0.7, 0.7, 1.0) | (0.1, 0.2, 0.2, 0.3) | 6 | 3.50×10 ⁻¹² | (0.36, 0.64, 0.67, 0.64) |
| Test 4 | (0.4, 0.7, 0.7, 1.0) | (0.2, 0.4, 0.4, 0.7) | 3 | 2.31×10 ⁻¹³ | (0.38, 0.72, 0.76, 0.95) |

| | Minimum density at each layer (g/cm ³) (1 st to 4 th layer) | Average density at each layer (g/cm ³) (1 st to 4 th layer) |
|--------|--|--|
| Test 1 | (0.23, 0.27, 0.34, 0.29) | (0.31, 0.34, 0.41, 0.35) |
| Test 2 | (0.42, 0.43, 0.51, 0.48) | (0.47, 0.50, 0.58, 0.55) |
| Test 3 | (0.32, 0.46, 0.33, 0.55) | (0.34, 0.55, 0.59, 0.58) |
| Test 4 | (0.33, 0.52, 0.57, 0.83) | (0.35, 0.59, 0.65, 0.91) |

110

(Page 12)

Table 2 Conditions and results for initial density model two.

| | True density (Trapezoid, Cuboid) (g/cm ³) | Initial density (Trapezoid, Cuboid) (g/cm ³) | Iterations (k) | RMS (E) | Maximum density (g/cm ³) | Minimum density (g/cm ³) | Average density (g/cm ³) |
|--------|--|---|-------------------|------------------------|---|---|---|
| Test 5 | (0.8, 1.0) | (0, 0) | 8 | 4.37×10 ⁻¹² | 0.6887 | 0.1328 | 0.4225 |
| Test 6 | (0.8, 1.0) | (0.2, 0.2) | 7 | 5.63×10 ⁻¹³ | 0.7121 | 0.1856 | 0.4886 |
| Test 7 | (0.8, 1.0) | (0.5, 0.5) | 5 | 1.06×10 ⁻¹³ | 0.7556 | 0.4762 | 0.6256 |
| Test 8 | (0.8, 1.0) | (-0.2, -0.2) | 13 | 8.49×10 ⁻¹¹ | 0.6399 | 0.0399 | 0.3276 |

- 3. (1) **359 IMPORTANT**“of the European Space Agency”. The webpage is not maintained by
115 **ESA and ESA is not responsible for that.**
- (2) **619** at the given website goce.mka.zcu.cz data cannot be browsed (how?), just it can be
downloaded? Please change the sentence if true.

Response: I really agree with the comments. The pages are web pages for ESA supported
120 project **Towards a better understanding of the Earth's interior and geophysical exploration
research "GOCE+ Geoexplore II"**, instead of ESA website. We have deleted the description and
provided the data website <http://goce.kma.zcu.cz/data.php>, which we have checked can be browsed.

Revision: (Page 16 Paragraph 1)

- 125 1. This study directly downloaded the preprocessed gravity gradient anomaly data with the spatial
resolution of 10 arc-min, which was acquired over 48 months from November 2009 to October 2013
(Sebera et al., 2014), from the website GOCE+ Geoexplore II (<http://http://goce.kma.zcu.cz/data.php>).

(Page 35)

- 130 2. The on-orbit GOCE gravity gradient data can be browsed and downloaded from GOCE+ Geoexplore
II (<http://goce.kma.zcu.cz/data.php>).

- 4. Section 3.6 - the text implies that this correction is due to the masses below the area of interest. This is was recently studied by Szwillus et al. (2016) showing the importance of lateral masses. Please mention this problem.

135

Response: Firstly, thanks a lot for recommending this important paper, which help us to know the exact extension criteria. We really have considered the long wavelength gravity gradient effect caused by the far zones, although we did not confirm the extended area (with 10° extension in all directions for far zone distant effects) is enough when we did this. The recommended paper points out that " For satellite-based gravity gradients, to reduce the remaining rms distant effect to 10% of the global rms, a radius of 10° is sufficient. And for the regional test, the RMS is much more smaller than the global average." Therefore , we confirm that 10° extension for far zone distant gravity gradient effects is enough for our study. We adopted the same method as the paper, **the extended geographic area within $E90^\circ$ – $E130^\circ$ and $N23^\circ$ – $N53^\circ$ is defined as the calculation area for corrections (Figure 13 e-f). And the obtained results in the study area are cut out from the calculation area.**

145

We made three revisions according to this problem. In revision 1, we described about the far zone distant gravity gradient effects before we did all the corrections. In revision 2, we added the two figures with extended area in Section 3.7, and these two figures (Topographic effects and underground interface undulation effects) also demonstrate that " Topographic and isostatic balance each other out to a certain degree" with the reference (Szwillus et al., 2016). In revision 3, for better understanding, we have changed the section title " long wavelength correction" to " Correction for the gravity gradient effects of the mantle under 180km".

150

Revision: (Page 18 Paragraph 1)

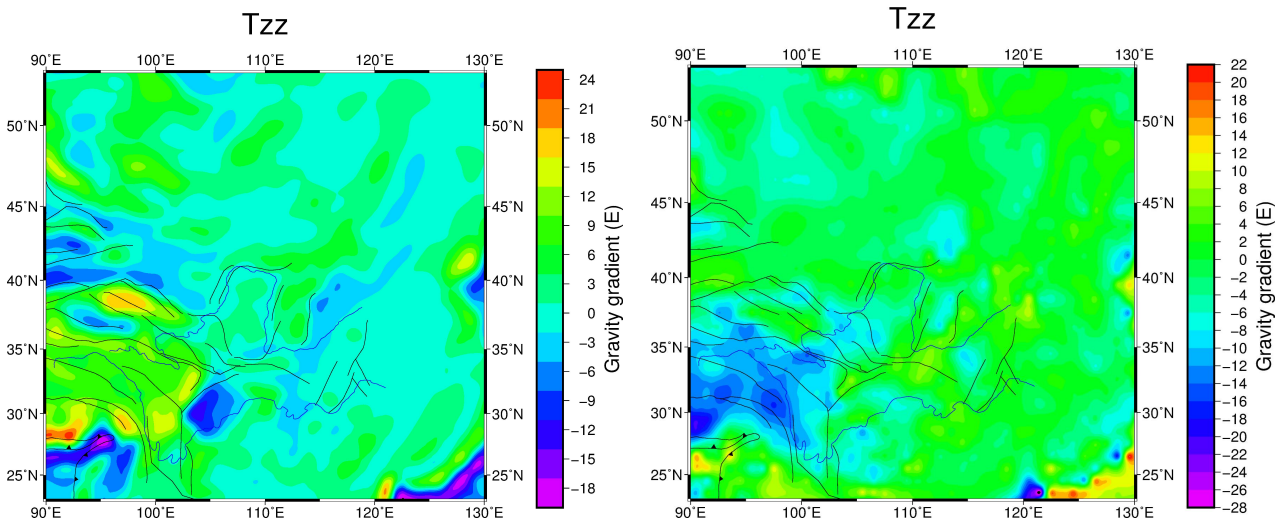
155

1. The gravity gradient anomaly components after downward continuation are a combination of the interface undulation and density heterogeneity. Thus, the topographic correction, underground interface undulation correction and long wavelength correction should be carried out in accordance with the existing precise models. These three corrections are affected by the masses within and outside the study area, the far-field correction outside the study area should be taken into consideration (Szwillus et al., 2016). Therefore, the correction radius in the study area is extended by 10° for all corrections. The same geographic area within $E90^\circ$ – $E130^\circ$ and $N23^\circ$ – $N53^\circ$ is defined as the calculation area for corrections (Figure 13 e-f). And the obtained results in the study area are cut out from the calculation area.

160

165

2. (Page 25)



170 **Figure 13** Gravity gradient effects with extended area (e) Topographic effects, (f) Interface undulation
(Sedimentary and Moho) effects.

3. (Page 23)

175 We changed the section title from " Long wavelength correction" to " Correction for the gravity
gradient effects of the mantle under 180km ".

Detailed questions

• 14 *Inconsistency* - do you mean a difference in the data representation (geometry)?

180

Response: We wanted to emphasize the different height between the observation planes , we have revised the sentence as following.

Revision: (Page 24 Paragraph 2)

185 Given the different bservation plane height between the on orbit GOCE satellite gravity gradient and
terrestrial gravity,

• 19 *performed* → applied to?

190 **Revision: (Page 1 Paragraph 2)**

Several essential corrections are **applied to** the four gravity gradient tensor

• **20 observation quantity** → **observations?**

195 **Revision: (Page 1 Paragraph 2)**

... after which the corrected gravity gradient anomaly (T'_{xx} , T'_{xz} , T'_{yy} , T'_{zz}) are used as the **observations**.

• **23-24 high heat flux ... could add a reference to this sentence?**

200 **Response:** We have added the reference to this sentence. We also added the temperature difference at 140km and 180km in Figure 15 (i, k) for better understanding.

Revision: (Page 1 Paragraph 3)

205 While in the mantle, the presented obvious low density areas are mainly affected by the high heat flux environment (**An and Shi, 2007**).

•(1) **36-38 please reformulate or leave this sentence "The most direct and effective approach..." because the following one repeats it in other words. Btw, the non-uniqueness of the gravity-based inversions make the gravity data not the easiest means for understanding the subsurface.** • (2) **38 variations - this little implies time variations. Please, reformulate.** • (3) **38 "laws"? Gravimetry does not study the laws behind measurements but it uses the laws to study phenomenas in the region of interest. Please reformulate**

215 **Response:** The original version is too cucumber, we have deleted the first sentence "The most direct and effective approach...", and shorten other two sentences as following.

Revision: (Page 2 Paragraph 1)

The gravity field data plays an important role in determining and interpreting the lithospheric density structure and state of motion.

220

• **49 Note ... gravity data contains all the frequencies about the whole Earth, but the high frequencies of the deep structures are just strongly attenuated due to the distance. If we would substantially improve S/N of the gravimeters, we could infer hi-freqs from the very deep density contrasts - the signal is there, just masked out by the signal of the closer masses. The point is**
225 **however that the data contains it all but due to the attenuation and the errors we do not have access to it.**

Response: Very constructive comments. We have reformulated the original sentences as following.

230 **Revision: (Page 2 Paragraph 1)**

In the frequency domain, the high frequencies of the deep structures are strongly attenuated due to the distance, and masked out by the signal of the closer masses, the gravity data can be mainly used to provide mid low frequency information of the deep structure.

235

• 60 *"rare"*? (please reformulate), search for the topic,
e.g. https://scholar.google.cz/scholar?hl=cs&as_sdt=0%2C5&q=joint+gravity+and+gradient+inversion&btnG=

240 **Response:** We wanted to emphasize the inversion realized in two steps, as we have changed the title from the "joint" to "sequential", we revised sentences as following.

Revision: (Page 2 Paragraph 2)

245 Currently, most researches based on the joint inversion of the gravity and gravity gradient data instead of the sequential inversion.

• (1) 120 the sentence "Since" does not make sense, please update
• (2) 121 *undetermined* is related to a number of data but you rather want to emphasize that the problem is ill-conditioned right?

250

Response: We revised the sentence as following, we emphasize the non-unique problem in the first sentence, and the ill-conditioned problem in the second sentence.

Revision: (Page 6)

255

The quantity of the unknowns m greatly exceeds the acquired data vector, the solutions of the equations are non-unique. Moreover, the inversion is an ill-conditioned problem, the appropriate constraints upon the objective function are required to narrow the range of solutions.

• 143 *"is comprehensive"* not clear what you mean (please reformulate)

260

Response: The word "comprehensive" is misleading, we used the word "complex" to replace comprehensive.

265 **Revision: (Page 7 Paragraph 1)**
"calculation of the Lagrangian multiplier is complex."

- 146 ?"...while a very small value may lead to a large ...the model and the data, thus providing unrealistic ..."??

270 **Response:** The sentence is misleading, we changed the sentences as following.

Revision: (Page 7 Paragraph 1)

275 Since the regularization parameter serves to balance the data fitting function and the model fitting function, an excessively large value will result in substantial differences between the inversed results response and the observation, while an overwhelmingly small value leads to the ineffectiveness of the model fitting function.

- 147 introduce the L-curve method before you write it is used

280 **Response:** We have reformulated the paragraph as following when we first introduced the L-curve.

Revision: (Page 7 Paragraph 2)

285 Given these problems, the L-curve method was developed for the selection of regularization parameters in the solution of ill-posed problems (Hansen, 1992). The L curve is a criterion that is based on a comparison between the actual data fitting function and the model objective function, which is applicable to solving problems with large scales. The value corresponding to the inflection point of the L curve is assigned to the regularization parameter. The effectiveness of this method has been validated in previous studies (Tian et al., 2018; 2019).

290 • 278 "... a more precise initial model" and/or more data, right?

Response: Right, we did not input the initial model in Figure 2b, but we input the different initial models in Figure 2c-2e. We have revised sentences as following.

295 **Revision: (Page 11 Paragraph 1)**

"... With the help of a more precise initial model and more data, Fig. 3b–d demonstrate that ...".

- 300 ...*decomposed into two integrated* ... → is composed of two steps?

300 **Revision: (Page 12)**

The sequential inversion is realized in two steps, namely, the gravity inversion and the gravity gradient inversion.

- 305 • (1) 335 What is meant by "outer" iterations. Are there any inner iterations so that these two have to distinguished in the paper ? (2) 455: "outer iterations"? (3) 202-228 Consider leaving the whole paragraph on PCG since this method is well described and established in the community. The paper is already quite long, here is the potential to shorten it.

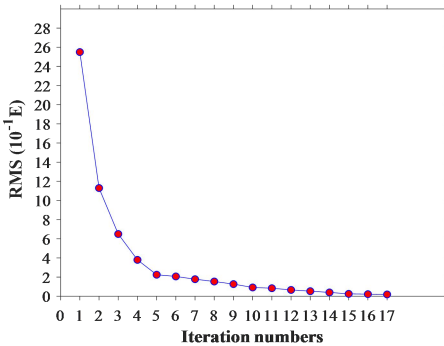
310 **Response:** The PCG algorithm consists of inner iteration and outer iteration. However, as we have left the whole paragraph on PCG algorithm and just provided the reference, we will not discriminate inner iteration and outer iteration in the revised version. We have used the term "iteration" to replace "outer iteration" throughout the paper.

- **Figure 5:** the red line is hardly visible, maybe not needed in this figure.

315

Response: We have updated both Figure 5 (b) and Figure 14, and deleted all the red line as following.

Revision: (Page 14)



320

- **Figure 6:** density distribution variation (it is not a full value right?)

Response: We have revised the Figure 6 caption as following.

325 **Revision: (Page 16)**

Figure 6 Lithospheric density distribution of NCC by gravity at different depths.

- **Figure 9:** update the caption, it is not clear what the panel (e) is showing (a 3D

map or T_{zz} as written in the title?)

330 **Response:** In Figure 9、Figure 10 and Figure 11, as most figures are 2D, we want to try some new attempts for showing figures in 3D form intuitively for better understanding. We want to show the topography/interface undulation and gravity gradient effects in one figure. The undulation of the figure represents topography or interface undulation, and the color reflects the corresponding gravity gradient effects T_{zz} . We have updated the figure with unit as following.

335 **Revision: (Page 19)**

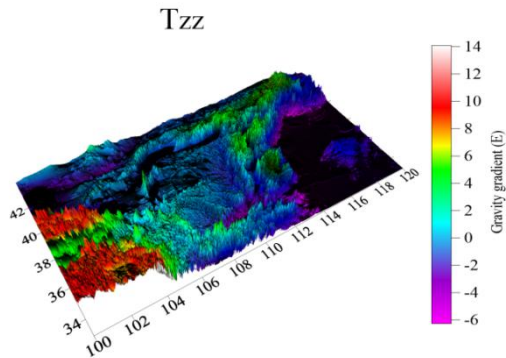


Figure 9 (e) The 3D gravity gradient effect T_{zz} of topography.

• **Figure 10 the same for (g), update unit in the colorbar of this panel (g). Shorten the caption as the caption repeats all the same (you can put "anomalous gravity gradients T_{xx} , T_{yy} ...etc" into one sentence)**

340

Response: We have checked all the figure captions. We have deleted the number in the panel and shortened all the captions, especially when we did not describe figures in detail. We have shortened the caption as following.

345

Revision: (Page 21)

Figure 10 (a) Sedimentary layer interface of the NCC. (b) Sedimentary layer interface undulation of the NCC. **The anomalous gravity gradient component caused by the relief at the sedimentary layer interface undulation, (c) T_{xx} , (d) T_{xz} , (e) T_{yy} , (f) T_{zz} . (g) The 3D gravity gradient effect T_{zz} of sedimentary layer interface undulation.**

350

• **421: You probably mean the gravity effect of the layer bounded by topo and Moho, right? The sentence implies to calculate the gravity effect of the Moho surface.**

355

Response: Right. We calculated the gravity gradient induced by Moho undulation instead of Moho surface. We have revised the paper as following.

Revision: (Page 21)

360 The Moho undulation after correcting for the average depth is illustrated in Fig. 11b. Similarly, the gravity gradient effects induced by the Moho undulation can be calculated.

• **442: what is meant by "relatively minor"? - the magnitudes are up to 1.5 E, which quite large**

365 **Response:** Right. We have deleted this sentence, and we have provided the statistics for all the corrections in Figure 13 (g-h) and Table 4, we really cannot ignore this correction based on the value.

• **Figure 12: remove "(a)...(d)" ...clear from the panels**

370 **Response:** We have updated all the figures in the paper, we only numbered the panel when we discussed some figures.

• **445: not clear what the sentence tries to tell (what official website, why this is linked with the accuracy/reliability of the data?)**

375

Response: We wanted to emphasize the spatial resolution of several models we used are different. We have revised paper as following.

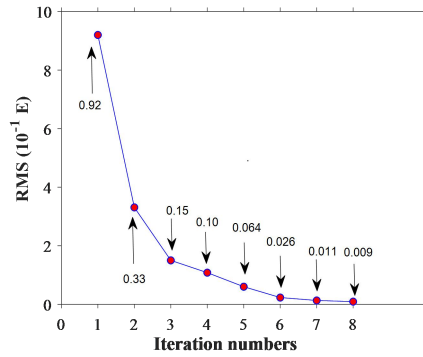
Revision: (Page 24)

380 "Since models with different spatial resolutions are used in several corrections, the spatial resolutions of the obtained results are different."

• **Figure 14: unit is missing in the y-axis**

385 **Response:** We have updated both Figure 5 (b) and Figure 14 with the unit "RMS ($10^{-1}E$)".

Revision: (Page 14 and Page 27)



390 **Figure 14** With the iterative calculation, residual mean square between the forward calculated theoretical gravity gradient and the gravity gradient measurements versus iteration number in the PCG inversion algorithm.

• 470: "*negative density anomalies*" → **negative density contrast/residuals?**

395 **Response:**

When we mentioned the specific value, we revised all the "*negative density anomalies*" → "negative density residuals", and "*positive density anomalies*" → "positive density residuals".

400

405

410

Sequential inversion of GOCE satellite gravity gradient data and terrestrial gravity data for the lithospheric density structure in the North China Craton

Yu Tian^{1,2,3}, Yong Wang^{2,3}

415 ¹Ocean College, Minjiang University, 350108 Fuzhou, China

²State Key Laboratory of Geodesy and Earth's Dynamics, Institute of Geodesy and Geophysics, Chinese Academy of Sciences, 430077 Wuhan, China

³University of Chinese Academy of Sciences, 100049 Beijing, China

Correspondence to: Yu Tian (tybgys455429145@163.com)

420 **Abstract.** The North China Craton (NCC) is one of the oldest cratons in the world. Currently, the destruction mechanism and geodynamics of the NCC still remain controversial. All of the proposed views regarding the issues involve studying the internal density structure of the NCC lithosphere. Gravity field data are one of the most important data in regard to investigating the lithospheric density structure, the gravity gradient data and the gravity data possess their own advantages.

Given the different observation plane height between the on orbit GOCE satellite gravity gradient and terrestrial gravity, also effects of the initial density model upon inversion results, the sequential inversion of gravity gradient and gravity are divided into two integrated processes. By using the preconditioned conjugate gradient (PCG) inversion algorithm, the density data are calculated using the preprocessed corrected gravity anomaly data. The newly obtained high resolution density data are then used as the initial density model, which can be served as the constraints for the subsequent gravity gradient inversion. Several essential corrections are applied to the four gravity gradient tensor (T_{xx} , T_{xz} , T_{yy} , T_{zz}) of the GOCE satellite, after which the corrected gravity gradient anomaly (T'_{xx} , T'_{xz} , T'_{yy} , T'_{zz}) are used as the observations. The result of lithospheric density distribution within the depth range of 0–180km in NCC is obtained.

The inversion results show followings. In the crust, the eastern NCC is affected by the lithosphere thinning with obvious local features. While in the mantle, the presented obvious negative density areas are mainly affected by the high heat flux environment (An and Shi, 2007). In the eastern NCC, the density anomaly in the Bohai Bay area is mostly attributed to the extension of the Tancheng-Lujiang major fault at the eastern boundary. In the western NCC, the crustal density anomaly distribution of the Qilian block is consistent with the northwest-southeast strike of the surface fault belt, whereas such an anomaly distribution experiences a clockwise rotation nearly to the north-south direction when it enters the mantle.

440

1 Introduction

The North China Craton (Fig. 1) is considered to be an outstanding example of cratons that has undergone both reconstruction and destruction. Studies on the NCC have provided us with opportunities to understand its formation and evolution, stabilization and destruction of the ancient continent. Two dominant destruction mechanisms of the NCC have been proposed, namely, delamination (Gao et al., 2009) and thermal erosion (Zhu et al., 2012). However, both of these mechanisms involve internal tectonic deformation and substance distribution of the lithosphere in the NCC, which highlights the utmost importance of obtaining the high resolution density structure of the lithosphere. **The gravity field data plays an important role in determining and interpreting the lithospheric density structure and state of motion.** For studies on the density structure of the NCC, Fang (1996) managed to invert the density distribution of the lithosphere in the North China area, with the constrained least square method using the Bouguer anomaly. Also using the Bouguer gravity anomaly, Wang et al. (2014) obtained the three-dimensional density structure of the NCC lithosphere through algebraic reconstruction inversion method, which was constrained by the seismic travel time. Based on the gravity, geoidal surface and topography data, Xu et al. (2016) calculated the crustal density and depth of the interface between the lithosphere and asthenosphere by the rapid integrated inversion method. Using the preprocessed data of the GOCE satellite gravity gradient anomaly, Tian and Wang (2018) constructed a three-dimensional density structure within the depth range of 0–120 km of the NCC lithosphere, during which the density variation induced by the temperature differences was incorporated. Previous studies on the NCC only adopted the gravity or gravity gradient measurements, both of which have their own unique advantages as the first order and second order derivatives of the gravity potential, respectively. **In the frequency domain, the high frequencies of the deep structures are strongly attenuated due to the distance, which are masked out by the signal of the closer masses, the gravity data can be mainly used to provide mid low frequency information of the deep structure.** And the amplitude of the gravity gradient data declines rapidly with an increasing depth of the field source, which demonstrates that the gravity gradient anomaly is applicable to the high frequency signal information of the shallow structure, characterized by short wavelengths. By using both the gravity and gravity gradient data as the observation quantities, the low frequency signal information of the gravity anomaly data and the high frequency signal information of the gravity gradient anomaly data can **expand** the frequency of the gravity field data. Sequential inversion of the gravity and gravity gradient data is able to achieve a mutual supplementation, which is favourable to enhance the reliability of the inversion result and obtain more reasonable analysis of the inversion solutions.

Currently, most researches based on the joint inversion of the gravity and gravity gradient data instead of the sequential inversion. Zhdanov et al. (2004) introduced the concept of the curvature of gravity to carry out an joint inversion of gravity and gravity gradient data, and applied proposed method to the existing models. Wu et al. (2013) **inverted** gravity and gravity gradient by transforming the formulas of the gravity and gravity gradient with the target body treated as a mass point. Given the varied decline rates of the kernel functions of the gravity and gravity gradient data, Capriotti and Li (2014) balanced the two decline rates with the help of the density matrix to conduct an joint inversion of the gravity and gravity gradient data,

475 after which the validity of the proposed method is confirmed using the published SEG model. Qin et al. (2016) developed the integrated focusing inversion algorithm of the gravity and gravity gradient data, and applied this method to the gravity and gravity gradient data of the aerial survey in Vinton salt dome area. Li et al. (2017) inverted the lithospheric three-dimensional density structure of the Qinghai-Tibet Plateau and its adjacent area within a depth range of 0–120 km using the gravity gradient data measured by the GOCE L2 together with the vertical gravity calculated via the EGM2008. In
480 the case of small research areas, studies involving gravity and gravity gradient joint inversion focused on the applications of the existing models or the aerial gravity and gravity gradient data at the same height. With respect to previous studies covering a large area, researchers often adopted gravity or gravity gradient data directly computed by the gravity field model. Although the gravity field model is able to rapidly calculate the gravity and gravity gradient data for large research areas all around the world, the resulting data are based on the spherical harmonic coefficients instead of actual measurements. Besides,
485 using the observations directly, rather than gravity field models, has the advantage of avoiding the global average effect during gravity field modeling (Pavlis et al., 2012). Thus, compared with the calculated data based on the gravity field model, the high precision gravity and gravity gradient data obtained from measurements with high resolution possess same importance (Liu et al., 2003; Li et al., 2011).

490 We selected GOCE satellite gravity gradients data along the orbit and gravity data of terrestrial survey as the measurements. The GOCE satellite data at the mean orbital height only reflects large structures of the earth. In order to highlight the high frequency information of shallow abnormal bodies and the detailed information of structural features, it is necessary to downward the GOCE satellite data from the mean orbital height to the near surface in NCC area. However, given the feasibility of the downward continuation result of the gravity gradient data from the GOCE satellite, the height of the
495 observation plane after the downward continuation should be located outside the topographic mass unit (Sebera et al., 2014; Li et al., 2017; Tian and Wang, 2018), while the each observation spot for gravity data acquired through the survey is always located on the topography surface. Therefore, a problem of inconsistency in the observation plane height is anticipated between the processed GOCE satellite gravity gradient data and the gravity data obtained by the terrestrial survey. Furthermore, although gravity and gravity gradient data are favoured by higher resolutions and sensitivity to density, the
500 inversion method is characterized by a strong non-uniqueness of solutions. For the purposes of constraining the gravity and gravity gradient inversion, seismic data are often input into the inversion after a transformation based on empirical formulas to suppress the non-uniqueness of solutions. In this regard, the effects of the initial model upon the inversion results should be taken into consideration. For the two aforementioned aspects, the sequential inversion of gravity and gravity gradient are divided into two processes. First, the density data converted from the seismic wave velocity are used as the initial density
505 model. The corrected gravity anomaly data of the terrestrial survey in NCC after preprocessing are collected as the observation quantity, then the density anomaly within a depth range of 0–180 km is calculated using the preconditioned conjugate gradient (PCG) algorithm at the first process. The obtained inversion results are used as the new initial density model, serving as constraints. The four high accuracy (Rummel et al., 2011; Yi et al., 2013) GOCE satellite gravity gradient

anomaly tensors (T_{xx} , T_{xz} , T_{yy} , T_{zz}) in NCC are collected as the original observation data for downward continuation, topographic effect correction, underground interface undulation effect correction and long wavelength correction. The preprocessed corrected gravity gradient anomaly data (T'_{xx} , T'_{xz} , T'_{yy} , T'_{zz}) are used as the new observation quantity, the resulting density anomaly distribution within the depth range of 0–180 km in this area are obtained using the same PCG algorithm at the second process.

By considering the features of gravity anomaly and gravity gradient anomaly data, we used the corrected gravity data as the initial measurements instead of gravity gradient data, which can be used to determine major and deep structures of the lithosphere by the inversion results firstly. Then the inversion results of corrected gravity gradient data is applied to identify fine structures of the lithosphere. This presented method can be exempt from the limitation imposed by the observation plane height, which is able to sufficiently exploit and utilize the available actual gravity and gravity gradient measurements. The corrected initial model with the effect of the gravity inversion results can provide the more reliable and effective initial density models for the following gravity gradient inversion. Compared with the inversion results based on either the gravity or gravity gradients in the NCC, the integrated inversion results offers both regional details information and density structure model penetrating deeper underground, which is favourable for discussions and analysis of data about the crust and mantle in the same area, consequently, investigating the phenomenon and origin of the destruction mechanism of the NCC.

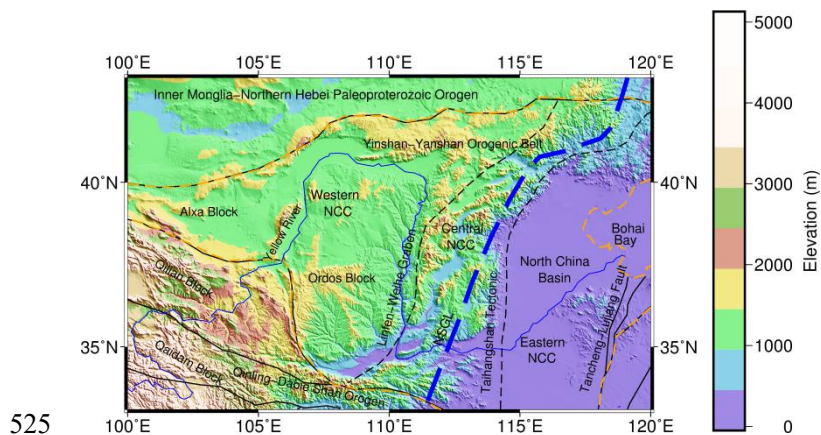


Figure 1 Topography and main tectonics of the study area. NCC - North China Craton.

2 Methods

2.1 Kernel function calculation

530 Under the Cartesian coordinate system, according to the geological body with the residual density of ρ and the volume of V , the first and second derivatives of the gravitational potential at any point $P_1 (x_0, y_0, z_0)$ in the outer space can be expressed as follows (Nagy et al. 2000):

$$\begin{aligned}
 T_z(P_1) &= G\rho \iiint \frac{(z-z_0)}{[(x-x_0)^2 + (y-y_0)^2 + (z-z_0)^2]^{3/2}} dx dy dz \\
 T_{xx}(P_1) &= G\rho \iiint \frac{2(x-x_0)^2 - (y-y_0)^2 - (z-z_0)^2}{[(x-x_0)^2 + (y-y_0)^2 + (z-z_0)^2]^{5/2}} dx dy dz \\
 T_{xz}(P_1) &= G\rho \iiint \frac{3(x-x_0)(z-z_0)}{[(x-x_0)^2 + (y-y_0)^2 + (z-z_0)^2]^{5/2}} dx dy dz \\
 T_{yy}(P_1) &= G\rho \iiint \frac{2(y-y_0)^2 - (x-x_0)^2 - (z-z_0)^2}{[(x-x_0)^2 + (y-y_0)^2 + (z-z_0)^2]^{5/2}} dx dy dz , \\
 T_{zz}(P_1) &= G\rho \iiint \frac{2(z-z_0)^2 - (x-x_0)^2 - (y-y_0)^2}{[(x-x_0)^2 + (y-y_0)^2 + (z-z_0)^2]^{5/2}} dx dy dz
 \end{aligned} \tag{1}$$

535 where G is the Newtonian gravitational constant. By dividing the underground space of the detection area into k prisms with the same size, each cube is given a particular residual density, the analytical expression of Eq.(1) can be expressed as:

$$\begin{aligned}
 T_z(P_1) &= \sum_{i=1}^k G\rho_i \left\{ (x-x_0) \ln[r + (y-y_0)] + (y-y_0) \ln[r + (x-x_0)] - (z-z_0) \arctan \frac{(x-x_0)(y-y_0)}{(z-z_0)r} \right\} \Big|_{x_i}^{x_{i+1}} \Big|_{y_i}^{y_{i+1}} \Big|_{z_i}^{z_{i+1}} = \mathbf{G}_z^{(P_1)} \boldsymbol{\rho} \\
 T_{xx}(P_1) &= \sum_{i=1}^k G\rho_i \left[-\tan^{-1} \frac{(y-y_0)(z-z_0)}{(x-x_0)r} \right] \Big|_{x_i}^{x_{i+1}} \Big|_{y_i}^{y_{i+1}} \Big|_{z_i}^{z_{i+1}} = \mathbf{G}_{xx}^{(P_1)} \boldsymbol{\rho} \\
 T_{xz}(P_1) &= \sum_{i=1}^k G\rho_i \ln(y-y_0+r) \Big|_{x_i}^{x_{i+1}} \Big|_{y_i}^{y_{i+1}} \Big|_{z_i}^{z_{i+1}} = \mathbf{G}_{xz}^{(P_1)} \boldsymbol{\rho} \\
 T_{yy}(P_1) &= \sum_{i=1}^k G\rho_i \left[-\tan^{-1} \frac{(z-z_0)(x-x_0)}{(y-y_0)r} \right] \Big|_{x_i}^{x_{i+1}} \Big|_{y_i}^{y_{i+1}} \Big|_{z_i}^{z_{i+1}} = \mathbf{G}_{yy}^{(P_1)} \boldsymbol{\rho} , \\
 T_{zz}(P_1) &= \sum_{i=1}^k G\rho_i \left[-\tan^{-1} \frac{(x-x_0)(y-y_0)}{(z-z_0)r} \right] \Big|_{x_i}^{x_{i+1}} \Big|_{y_i}^{y_{i+1}} \Big|_{z_i}^{z_{i+1}} = \mathbf{G}_{zz}^{(P_1)} \boldsymbol{\rho}
 \end{aligned} \tag{2}$$

where $\mathbf{G}_z^{(P_1)}, \mathbf{G}_{xx}^{(P_1)}, \mathbf{G}_{xz}^{(P_1)}, \mathbf{G}_{yy}^{(P_1)}, \mathbf{G}_{zz}^{(P_1)}$ represents the corresponding kernel function matrix at the point P_1 ,

540 $\boldsymbol{\rho} = (\rho_1, \rho_2, \dots, \rho_k)^T$ represents the density of each cube. The gravity gradient anomalies generated by all the n points on the observation surface meet the linear relationship from the k discrete prisms in the underground space. The relationship can be expressed as the equation:

$$\begin{aligned}
 \mathbf{T}_{ij} &= \mathbf{G}_{ij} \boldsymbol{\rho} , \\
 \mathbf{T}_{ij} &= [\mathbf{T}_{ij}^{(P_1)}, \mathbf{T}_{ij}^{(P_2)}, \dots, \mathbf{T}_{ij}^{(P_n)}]^T , \\
 \mathbf{G}_{ij} &= [\mathbf{G}_{ij}^{(P_1)}, \mathbf{G}_{ij}^{(P_2)}, \dots, \mathbf{G}_{ij}^{(P_n)}]^T , \quad ij = z, xx, xz, yy, zz
 \end{aligned} \tag{3}$$

where T_{ij} represents the observation, G_{ij} represents the corresponding kernel function matrix for the observation surface.

545 2.2 Inversion method

The inversion of the gravity and gravity gradient tensors is, in essence, a process of solving a system of linear equations. The quantity of the unknowns m greatly exceeds the acquired data vector, the solutions of the equations are non-unique. Moreover, the inversion is an ill-conditioned problem, the appropriate constraints upon the objective function are required to narrow the range of solutions. Therefore, in the linear inversion theory, the objective function mostly consists of the data fitting function and the model objective function (Constable et al., 1987). Under such circumstances, solving the inversion problem is equivalent to finding a model vector m that is able to minimize the objective function while satisfying the data fitting function condition.

The objective function can be expressed as:

$$555 \text{ minimize: } \phi = \phi_d + \mu\phi_m, \quad (4)$$

where μ represents the regularization parameter, which stands for the weight factor that balances the data fitting function ϕ_d and the model objective function ϕ_m .

The data fitting function is defined as below:

$$560 \phi_d = \sum_{i=1}^N \left(\frac{\Delta d_i - G_i \Delta m}{\sigma_i} \right)^2 = \|W_d(\Delta d - G\Delta m)\|^2, \quad (5)$$

$$W_d = \text{diag} \{1/\sigma_1, 1/\sigma_2, \dots, 1/\sigma_N\}, \quad (6)$$

where $\Delta m = m - m_0$ is the correction between the model parameter vector m and the initial model m_0 ; G is the kernel function, namely, the linear projection operator from the model element to the observation (for gravity data, $G = G_z$, while for gravity gradient components, $G = [G_{xx}, G_{xz}, G_{yy}, G_{zz}]^T$); Δd is the correction of the corresponding measurement; and W_d is a diagonal matrix, with σ_i representing the standard deviation of the i -th data. The objective function of the model is constructed according to the minimization model function.

The Lagrangian multiplier is used as the regularization parameter in the PCG inversion algorithm. In the process of solving a large scale matrix, calculation of the Lagrangian multiplier is complex, therefore, an empirical value is often adopted as the relative optimal value for the regularization parameter. Since the regularization parameter serves to balance the data fitting function and the model fitting function, an excessively large value will result in substantial differences between the inversed

results response and the observation, while an overwhelmingly small value leads to the ineffectiveness of the model fitting function.

575 Given these problems, the L-curve method was developed for the selection of regularization parameters in the solution of
 580 ill-posed problems (Hansen, 1992). The L-curve is a criterion that is based on a comparison between the actual data fitting
 function and the model objective function, which is applicable to solving problems with large scales. The value
 corresponding to the inflection point of the L-curve is assigned to the regularization parameter. The effectiveness of this
 method has been validated in previous studies (Tian et al., 2018; 2019). The curvature of the L-curve can be expressed as
 (Hansen, 1992):

$$k = \frac{\hat{\rho}'\hat{\eta}'' - \hat{\rho}''\hat{\eta}'}{[(\hat{\rho}')^2 + (\hat{\eta}')^2]^{3/2}}, \quad (7)$$

where $\hat{\rho} = \log(\phi_d)$, $\hat{\eta} = \log(\phi_m)$; and the superscripts ' and '' represent the first-order and second-order derivatives of the
 function, respectively. Accordingly, during the inversion process, the algorithm seeks the maximum curvature of the L-curve
 based on the function constructed by actual data.

585 To constrain the spatial structure of the model and achieve a continuous variation of the inversion image along the three axis
 directions, a roughness matrix is introduced into the model objective function (Constable et al., 1987), with reference to the
 minimization model function. The three-dimensional model vector \mathbf{R} is the quadratic sum of the first-order partial difference
 of the model vector \mathbf{m} along the x, y and z directions.

$$590 \quad \mathbf{R} = \|\partial_x \Delta \mathbf{m}\|^2 + \|\partial_y \Delta \mathbf{m}\|^2 + \|\partial_z \Delta \mathbf{m}\|^2 = \int \left(\frac{\partial \Delta \mathbf{m}}{\partial x} \right)^2 dv + \int \left(\frac{\partial \Delta \mathbf{m}}{\partial y} \right)^2 dv + \int \left(\frac{\partial \Delta \mathbf{m}}{\partial z} \right)^2 dv, \quad (8)$$

by meshing the model and replacing the partial differential form with the finite difference form, the above equation is
 converted into the matrix:

$$\mathbf{R} = \Delta \mathbf{m} (\mathbf{R}_x^T \mathbf{R}_x + \mathbf{R}_y^T \mathbf{R}_y + \mathbf{R}_z^T \mathbf{R}_z) \Delta \mathbf{m}, \quad (9)$$

where \mathbf{R}_x , \mathbf{R}_y and \mathbf{R}_z are the roughness matrices of the model along the x, y and z directions, respectively.

595 Because the gravity data and gravity gradient data has no fixed depth resolution, the kernel function declines rapidly with an
 increasing depth, and the inversion results are limited near the surface, which results in difficulties in capturing the true
 position of the anomaly. By introducing the depth weighting function into the model objective function, the kernel function
 is optimized to reflect the true weighted value of the anomaly element at each depth. The depth weighting function designed
 600 by Li and Oldenburg (1996) especially for the inversion of gravity data and gravity gradient data is adopted:

$$W(z) = \frac{1}{(Z + Z_0)^{\beta/2}}, \quad (10)$$

where Z is the burial depth of the centre of the grid cell; Z_0 and β are constants. For gravity data, these values are used to counteract the decline in the kernel function \mathbf{G} , with β often set to 2 and the function written as $(Z+Z_0)^{-1}$, while for gravity
605 gradient data, these values are used to compensate the decline in the kernel function \mathbf{G} , with β often set to 3 and the function written as $(Z+Z_0)^{-3/2}$.

In accordance with the minimization model function, the model objective function can be constructed as shown below, in reference to the roughness matrix and depth weighting function:

$$\phi_m(\mathbf{m}) = \alpha_s \int_V (\partial W(z) \Delta \mathbf{m})^2 dv + \alpha_x \int_V \left(\frac{\partial W(z) \Delta \mathbf{m}}{\partial x} \right)^2 dv + \alpha_y \int_V \left(\frac{\partial W(z) \Delta \mathbf{m}}{\partial y} \right)^2 dv + \alpha_z \int_V \left(\frac{\partial W(z) \Delta \mathbf{m}}{\partial z} \right)^2 dv, \quad (11)$$

610

the model objective function can be converted into the matrix form by replacing the differential form with the finite difference method:

$$\phi_m(\mathbf{m}) = \Delta \mathbf{m}^T (\mathbf{W}_S^T \mathbf{W}_S + \mathbf{W}_x^T \mathbf{W}_x + \mathbf{W}_y^T \mathbf{W}_y + \mathbf{W}_z^T \mathbf{W}_z) \Delta \mathbf{m} = \Delta \mathbf{m}^T \mathbf{W}_i^T \mathbf{W}_i \Delta \mathbf{m}, \quad (12)$$

$$\mathbf{W}_i = \alpha_i \mathbf{R}_i \mathbf{D}, \quad i = s, x, y, z, \quad (13)$$

where α_i is the weight coefficient for each term in the objective function; \mathbf{R}_i is the difference operator for each
615 component; and \mathbf{D} is the discretized depth weighting function matrix. Substituting the model objective function into the objective function yields:

$$\phi = (\Delta \mathbf{d} - \mathbf{G} \Delta \mathbf{m})^T (\Delta \mathbf{d} - \mathbf{G} \Delta \mathbf{m}) + \mu \Delta \mathbf{m}^T \mathbf{W}_i^T \mathbf{W}_i \Delta \mathbf{m}, \quad (14)$$

Eq. (11) can be re-arranged into the form of matrix:

$$\begin{bmatrix} \mathbf{G} \\ \sqrt{k} \mathbf{W}_i \end{bmatrix} \Delta \mathbf{m} = \begin{bmatrix} \Delta \mathbf{d} \\ 0 \end{bmatrix} \quad (15)$$

620 by replacing the condition matrix of the objective function with $\mathbf{A} = \begin{bmatrix} \mathbf{G} \\ \sqrt{k} \mathbf{W}_i \end{bmatrix}^T$ and defining $\mathbf{b} = [\Delta \mathbf{d}, 0]^T$, Eq. (15) can be simplified as:

$$\mathbf{A} \Delta \mathbf{m} = \mathbf{b}, \quad (16)$$

for the gravity data, we take the \mathbf{T}_z as the observation, $\mathbf{A} = \begin{bmatrix} \mathbf{G}_z \\ \sqrt{\mu} \mathbf{W}_i \end{bmatrix}^T$ and $\mathbf{b} = [\mathbf{T}_z, 0]^T$, for the gravity gradient data, we selected four processed components \mathbf{T}'_{xx} 、 \mathbf{T}'_{xz} 、 \mathbf{T}'_{yy} and \mathbf{T}'_{zz} **simultaneously** as the observation, which implies

625 the Jacobian matrix $\mathbf{A} = [\mathbf{G}_{xx}, \mathbf{G}_{xz}, \mathbf{G}_{yy}, \mathbf{G}_{zz}, \sqrt{\mu} \mathbf{W}_i]^\top$ and $\mathbf{b} = [\mathbf{T}'_{xx}, \mathbf{T}'_{xz}, \mathbf{T}'_{yy}, \mathbf{T}'_{zz}, 0]^\top$. The contribution of each component and its differences from joint inversion can be referred to our previous studies (Tian et al., 2019).

Additionally, $\mathbf{A}^\top \mathbf{A} = (\mathbf{G}^\top \mathbf{G} + k^{-1} \mathbf{W}_i^\top \mathbf{W}_i)$. Because the condition number of the Jacobian matrix is normally very large, to increase the convergence speed and the solution stability, Eq. (16) is re-written as:

$$630 \quad \mathbf{S} \mathbf{A}^\top \mathbf{A} \Delta \mathbf{m} = \mathbf{S} \mathbf{A}^\top \mathbf{b}, \quad (17)$$

where \mathbf{S} is the preconditioned factor and is usually approximated as $(\mathbf{A}^\top \mathbf{A})^{-1}$. By doing this, the eigenvalues of Eq. (17) will be concentrated along the diagonal and the condition number will be improved so that the iteration efficiency is improved (Pilkington, 2009).

635 The PCG method is an algorithm for solving linear or nonlinear equations through an iterative calculation process and is mainly used to solve a quadratic equation $\phi = \frac{1}{2} \mathbf{m}^\top \mathbf{A} \mathbf{m} - \mathbf{m}^\top \mathbf{b}$, with the solution $\mathbf{m} = \mathbf{A}^{-1} \mathbf{b}$, which obviously is equivalent to Eq. (16). The PCG method (Pilkington, 1997; 2009) is adopted for the inversion calculation.

2.3 Effects of the initial density model

Two models (Fig. 2 and Fig. 3) are designed **in order to test the effects of the initial model upon the inversion results**. The model one (Fig. 2) consists of two independent cubes **equipped with density values**. The densities are different at each layer to study the role of the initial values in the inversion. The model two (Fig. 3) is composed of an upright cuboid and a trapezoid structure of multiple anomalies. This model test can be used to illustrate the initial model effects upon the shape and magnitude of the inversion results. Since this study aims to capture the initial model effects upon the final inversion results, carrying out the integrated inversion for the four components (\mathbf{T}_{xx} , \mathbf{T}_{xz} , \mathbf{T}_{yy} , \mathbf{T}_{zz}) is required.

645

As is shown in Fig. 2 and Fig. 3, the inversion has been carried out for the identical density anomaly bodies (Fig. 2a and Fig. 3a), during which the gravity gradient measurement, kernel function and algorithm parameters are all the same, except that the varied values are assigned to the initial model. In Model 1, the anomalies are set to 0 g/cm³ (Fig. 2b); 0.4 g/cm³ (Fig. 2c); 0.1 g/cm³ (the 1st layer), 0.2 g/cm³ (the 2nd and 3rd layers) and 0.3 g/cm³ (the 4th layer) in Fig. 2d; 0.2 g/cm³ (the 1st layer), 0.4 g/cm³ (the 2nd and 3rd layers) and 0.6 g/cm³ (the 4th layer) in Fig. 2e. Then, in Model 2, the initial densities are set as 0 g/cm³ (Fig. 3b), 0.2 g/cm³ (Fig. 3c), 0.5 g/cm³ (Fig. 3d) and -0.2 g/cm³ (Fig. 3e).

650

In terms of the inversion of Model 1, the iterations are 10, 7, 6 and 3, and the inversion results are illustrated in Fig. 2b-e. The detailed results of every inversion test are summarized in Table 1.

655

Table 1 Conditions and results for initial density model one.

| | True density at each layer (g/cm ³) (1 st to 4 th layer) | Initial density at each layer (g/cm ³) (1 st to 4 th layer) | Iterations (k) | RMS (E) | Maximum density at each layer (g/cm ³) (1 st to 4 th layer) |
|--------|--|--|-------------------|------------------------|--|
| Test 1 | (0.4, 0.7, 0.7, 1.0) | (0, 0, 0, 0) | 10 | 7.35×10^{-11} | (0.34, 0.42, 0.53, 0.55) |
| Test 2 | (0.4, 0.7, 0.7, 1.0) | (0.4, 0.4, 0.4, 0.4) | 7 | 6.94×10^{-12} | (0.51, 0.55, 0.66, 0.58) |
| Test 3 | (0.4, 0.7, 0.7, 1.0) | (0.1, 0.2, 0.2, 0.3) | 6 | 3.50×10^{-12} | (0.36, 0.64, 0.67, 0.64) |
| Test 4 | (0.4, 0.7, 0.7, 1.0) | (0.2, 0.4, 0.4, 0.7) | 3 | 2.31×10^{-13} | (0.38, 0.72, 0.76, 0.95) |
| | Minimum density at each layer (g/cm ³) (1 st to 4 th layer) | Average density at each layer (g/cm ³) (1 st to 4 th layer) | | | |
| Test 1 | (0.23, 0.27, 0.34, 0.29) | (0.31, 0.34, 0.41, 0.35) | | | |
| Test 2 | (0.42, 0.43, 0.51, 0.48) | (0.47, 0.50, 0.58, 0.55) | | | |
| Test 3 | (0.32, 0.46, 0.33, 0.55) | (0.34, 0.55, 0.59, 0.58) | | | |
| Test 4 | (0.33, 0.52, 0.57, 0.83) | (0.35, 0.59, 0.65, 0.91) | | | |

Fig. 2b–e indicate that as the initial model becomes more precise, the inversion results become more reliable, with the values of the anomalies become more similar to the true model. With no defined initial model (Fig. 2b), it is difficult to capture the layered structure of the anomaly and the resulting average density is only 0.38 g/cm³, which is far different from the true model, although in this case, the inversion results manage to capture the position of the anomaly, its depth distribution, and its shape as two upright cuboids. The whole inversion process is relatively time consuming and finally reaches the convergence criterion after 10 iterations. We also compare the cases based on Model 1 with one another. Compared with Fig. 2d, although Fig. 2c presents smaller differences of the density anomaly values from those of the true model, the layered structure of the anomaly is difficult to capture from Fig. 2c. In Fig. 2d, it is feasible to conclude that certain differences exist between the density anomaly distributions of the 1st and 2nd layers, which is more similar to the true model. This finding suggests that the inversion results are related not only to the density value of the initial model but also to the distribution structure of the initial density. Therefore, a more precise initial model with a layered density value distribution is in favour of generating more reliable inversion results. It should be noted that the optimal inversion results are attributed to the case of Fig. 2e, which produce an inverted anomaly body shape that is almost identical to the true model. Apparently, the density distribution of the anomaly body is laminated into 3 layers, with the 1st layer having a density anomaly of 0.3–0.4 g/cm³; the 2nd and 3rd layers generally having density anomalies of 0.6–0.7 g/cm³; and the 4th layer having a density anomaly of 0.8–1.0 g/cm³.

660

665

670

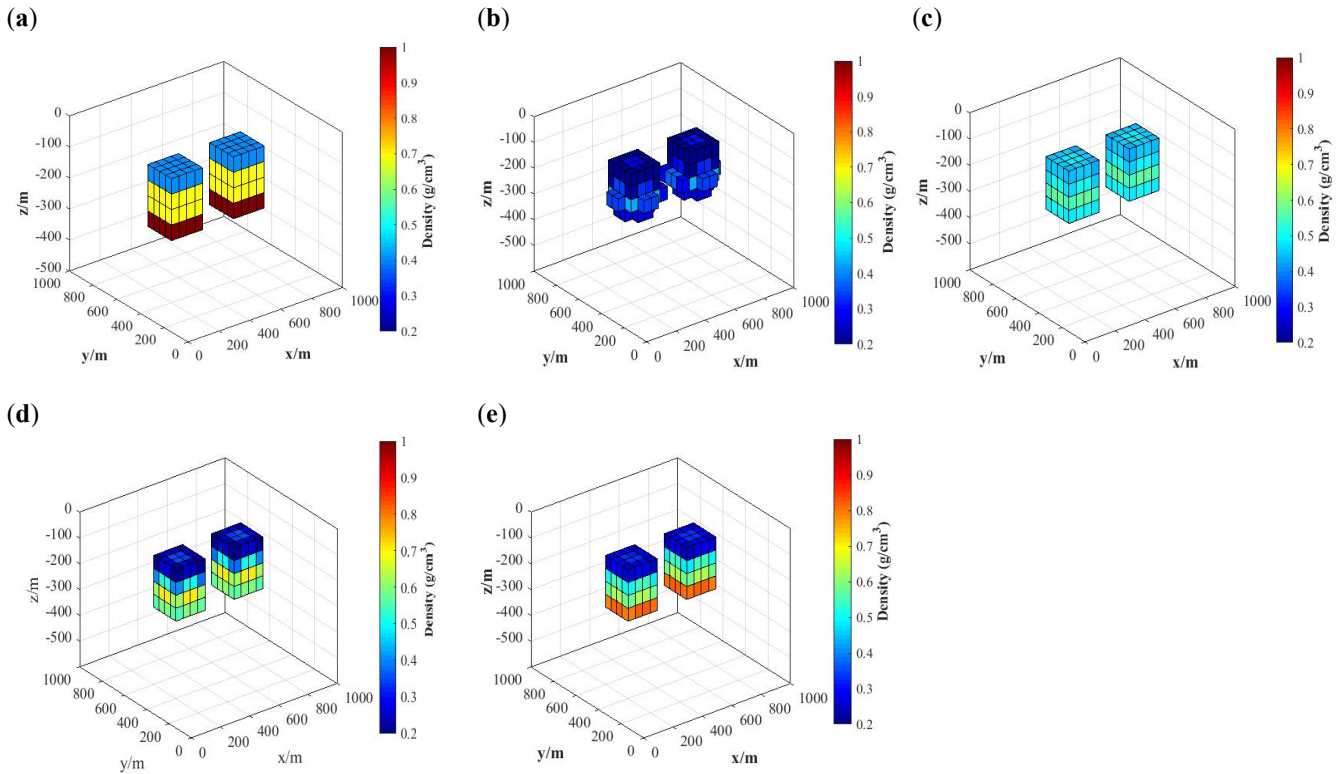


Figure 2 Initial density model experiments one. (a) True model. Inversion result (b) Test 1, (c) Test 2, (d) Test 3, (e) Test 4.

675

For Model 2, the inversion for each case is calculated after 8, 7, 5 and 13 iterations. The inversion results are illustrated in Fig. 3b–e, and the details of the results of each case are given in Table 2. **With the help of a more precise initial model and more data**, Fig. 3b–d demonstrate that it would be easier to determine the shape and dimensions of the density anomaly body from the inversion results. In the inversion results of Fig. 3b, it is feasible to directly capture the right upright cuboid of the density anomaly, and for the left complicated density anomaly body, the interpretation based on the inversion results is limited to this anomaly body having an irregular shape and its size growing with an increasing depth. In Fig. 3c, the left anomaly body reveals a stair-like shape, yet it is surrounded by multiple small anomaly bodies, and the density values of the right upright cuboid are closer to the true model. Next, the optimal inversion results are found in Fig. 3d, with the anomaly body shapes that are completely consistent with those of the true model, and it is easy to discriminate the shape of the anomaly body. Meanwhile, it should also be noted that the density anomaly value of the right upright cuboid is higher than that of the left stair-like body. Finally, the inversion results of Fig. 3e show difficulties in determining the shape and size of both of the anomaly bodies. In addition, according to the inversion results summary (Table 2), the average density anomaly in this case is only 0.3276 g/cm^3 , which is very different from the true model.

690

Table 2 Conditions and results for initial density model two.

| | True density (Trapezoid, Cuboid) (g/cm ³) | Initial density (Trapezoid, Cuboid) (g/cm ³) | Iterations (k) | RMS (E) | Maximum density (g/cm ³) | Minimum density (g/cm ³) | Average density (g/cm ³) |
|--------|--|---|-------------------|------------------------|---|---|---|
| Test 5 | (0.8, 1.0) | (0, 0) | 8 | 4.37×10^{-12} | 0.6887 | 0.1328 | 0.4225 |
| Test 6 | (0.8, 1.0) | (0.2, 0.2) | 7 | 5.63×10^{-13} | 0.7121 | 0.1856 | 0.4886 |
| Test 7 | (0.8, 1.0) | (0.5, 0.5) | 5 | 1.06×10^{-13} | 0.7556 | 0.4762 | 0.6256 |
| Test 8 | (0.8, 1.0) | (-0.2, -0.2) | 13 | 8.49×10^{-11} | 0.6399 | 0.0399 | 0.3276 |

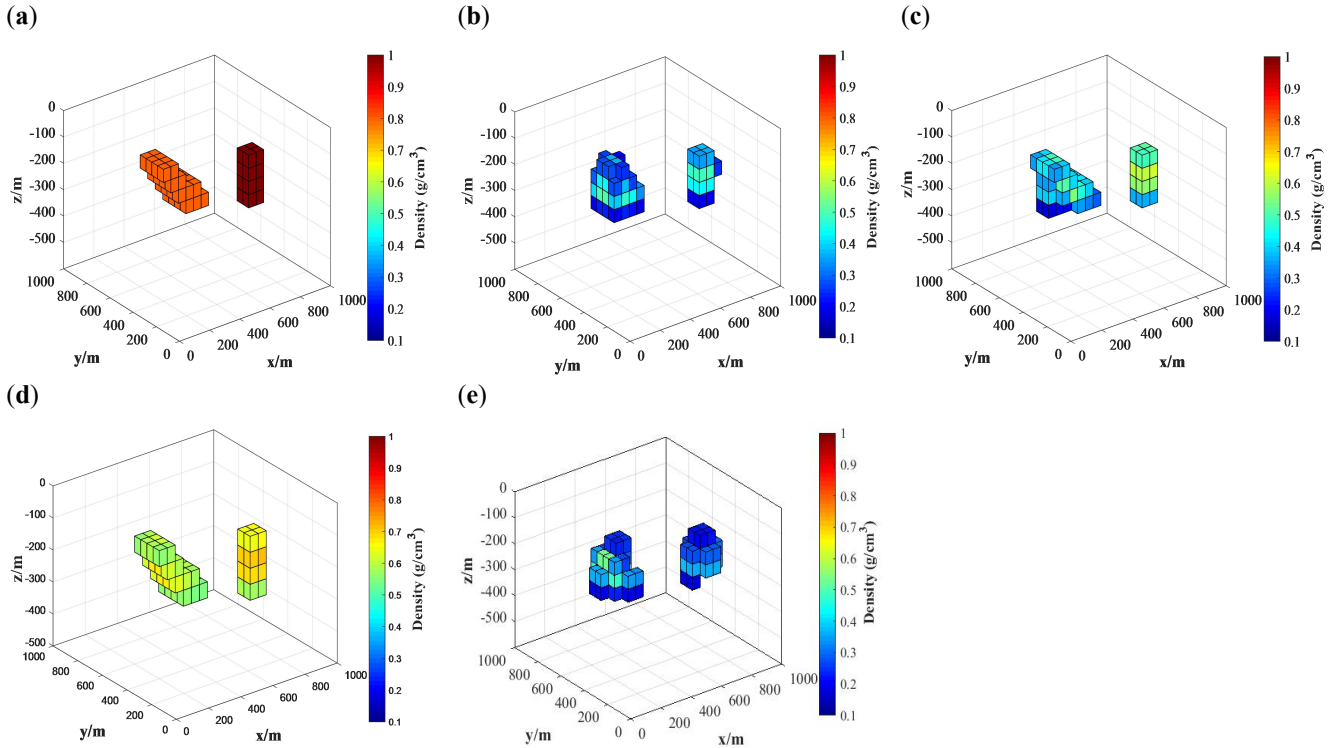


Figure 3 Initial density model experiments two. (a) True model. Inversion result (b) Test 1, (c) Test 2, (d) Test 3, (e) Test 4.

695 The model tests show that the inversion results are not only related to the observation, but also affected by the physical and geometric parameters of the initial density model. Therefore, the density values for the initial model, as well as the general area where the density anomaly body is located, should be set more accurate for the initial density model.

2.4 The process of the sequential inversion

The sequential inversion is realized in two steps, namely, the gravity inversion and the gravity gradient inversion. The detailed work-flow of the whole inversion process is illustrated in Fig. 4. Given the constraint imposed on the inversion

700

results by the initial density model, the results of the gravity inversion with high precision are used as the new initial density model for the subsequent steps, by which the ultimate inversion results are, to some extent, constrained during the gravity gradient inversion calculation. Specifically, the density data converted from the seismic wave velocity are first used as the initial density model, and the preprocessed corrected gravity anomaly data are collected to serve as the observation quantity. Then, the kernel function corresponding to the gravity data is calculated, and the density anomaly data within the depth range of 0–180 km in the study area are calculated through the PCG algorithm. Then, the obtained gravity inversion results are used as the new initial density model and the gravity gradient components of this area measured by the GOCE satellite are processed, after which the four corrected gravity gradient anomaly components (T'_{xx} , T'_{xz} , T'_{yy} , T'_{zz}) are used as the new observation simultaneously. The kernel functions corresponding to each gravity gradient component are calculated, and then the ultimate density anomaly distribution within a depth range of 0–180 km in the study area is obtained through the same PCG algorithm.

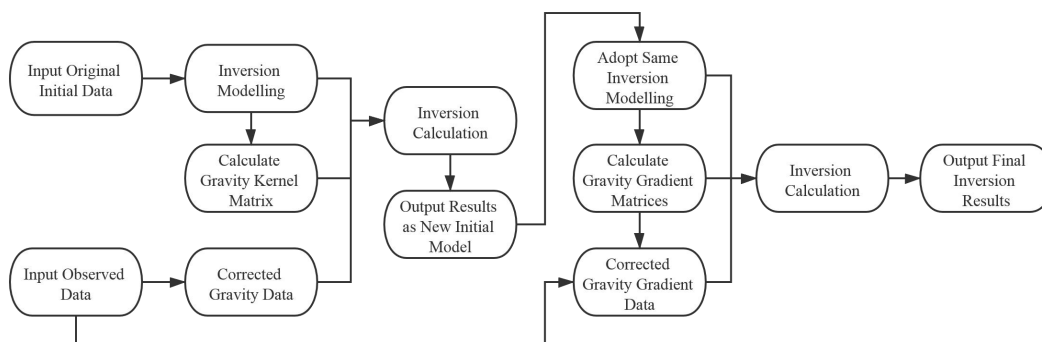


Figure 4 The flowchart of the whole procedure of the PCG inversion algorithm.

3 Data processing

3.1 Inversion based on the corrected gravity anomaly data

The corrected gravity anomaly data (Wang et al., 2012) with the depth 0-180km in NCC has been collected directly. The corrected gravity anomaly data is based on the $5' \times 5'$ free air gravity anomalies data set, which comes from China Seismic Network. The corrected gravity data has been dealt with topographic correction, Bouguer correction firstly; then the underground interface undulation correction which consists of sedimentary undulation correction and Moho undulation correction; and long wavelength correction which corresponds to the gravity gradient effects of 2nd–33th order spherical harmonic coefficients. The gravity anomalies induced by the density heterogeneity of the crust and upper mantle are used as the observation for inversion. The gravity anomaly (Fig. 5a) after multiple corrections are shown in Fig. 5a. The figure shows that the gravity anomaly of the eastern NCC is seen with alternating distributions of positive and negative anomalies, with local features. In the central NCC, most regions along the Taihang Orogenic belt and the Yinshan-Yanshan Orogenic

725 belt are found with negative gravity anomalies. For the western NCC, the whole Ordos block presents a prominent positive gravity anomaly distribution.

Although the gravity data are favoured by their higher resolutions, the gravity inversion suffers from a strong non-uniqueness of solutions. It is effective to introduce seismic data into the gravity inversion to constrain the gravity inversion process the non-uniqueness of solution. Based on the resolution of $0.5^\circ \times 0.5^\circ$ P-wave velocity structure obtained by seismic tomography (Tian et al., 2009), we constructed a three dimensional initial density model for the NCC lithosphere, using the empirical velocity to density conversion formula of the North China area (Eq. 16). The constructed models are divided into eight layers along the depth direction, with base depths of 10 km, 25 km, 42 km, 60 km, 80 km, 100 km, 140 km and 180 km. Along the horizontal direction, the model is meshed into grids of $0.5^\circ \times 0.5^\circ$. As shown in Fig. 5b, after 17 iterations, the curve of defined RMS misfit tends to be horizontal, the variation is slight, and the calculated RMS misfit of 8.2×10^{-3} was obtained, at which point the inverse iterative calculation was complete.

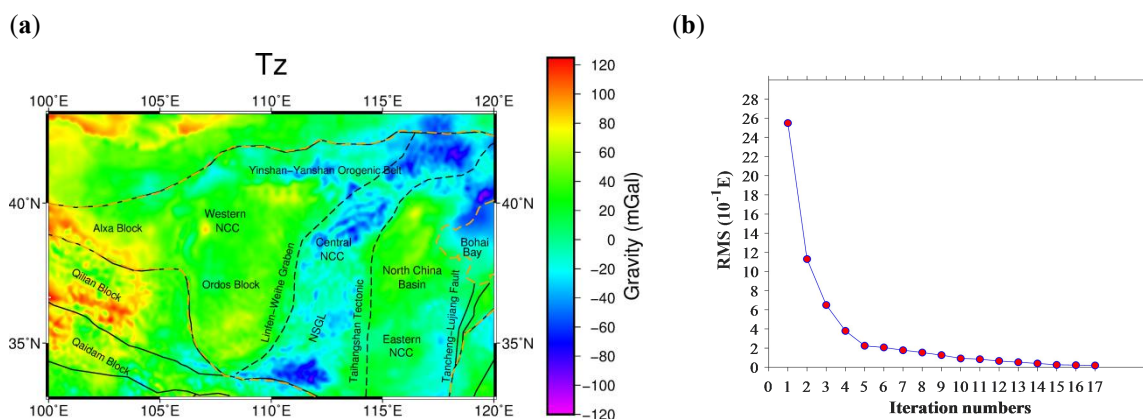
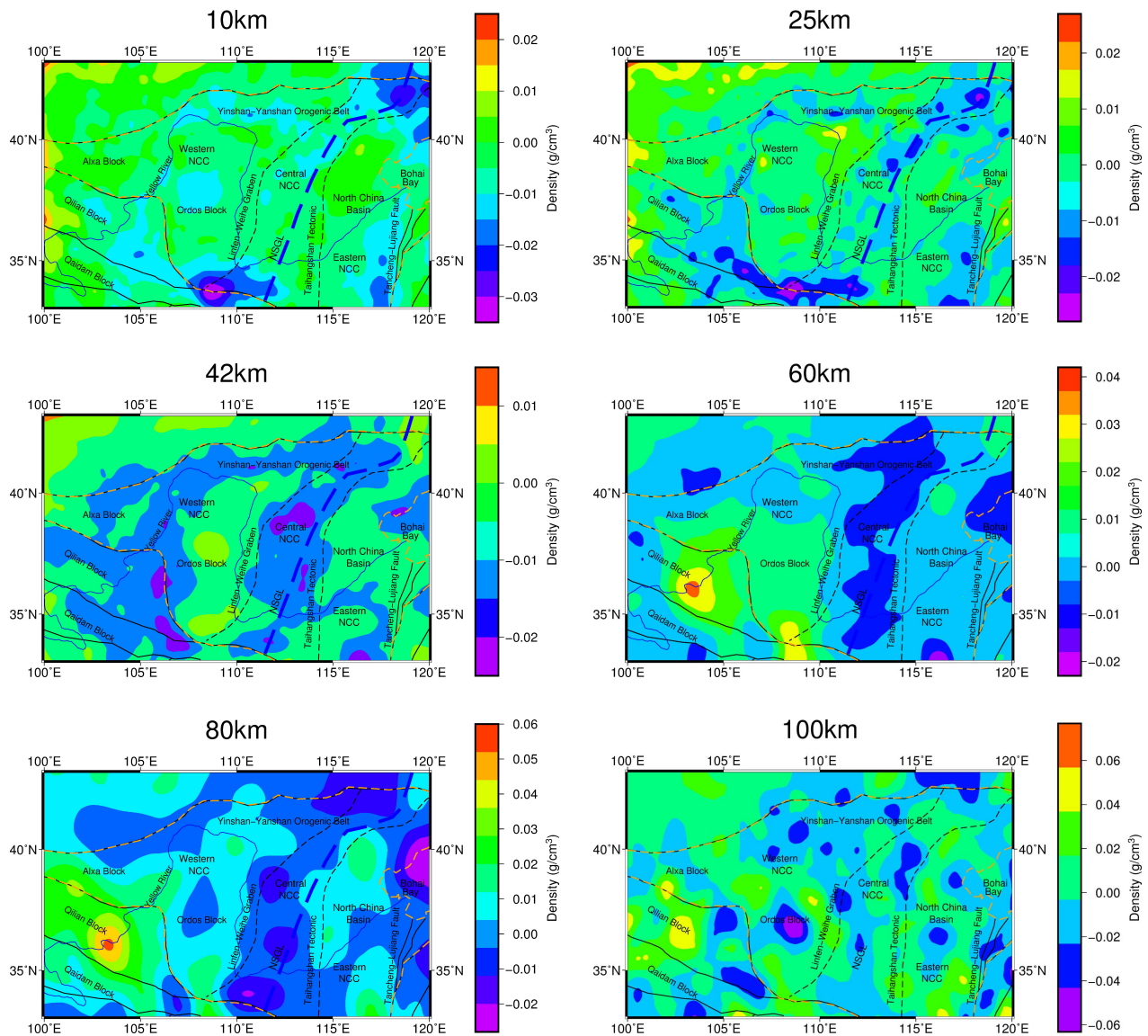


Figure 5 (a) The corrected gravity anomalies after several corrections. (b) With the iterative calculation, residual mean square between the forward calculated theoretical gravity and the gravity measurements versus iteration number in the PCG inversion algorithm.

740 The three-dimensional density anomaly distribution of the lithosphere within 0–180 km, which is meshed into $0.25^\circ \times 0.25^\circ$ cells (Fig. 6), has been inverted from the corrected gravity anomaly. The results are then used as the new initial model for the gravity gradient inversion. In Sect. 5, the results of the initial and final inversion results (Fig. 6 and Fig. 15) are further analysed and discussed.



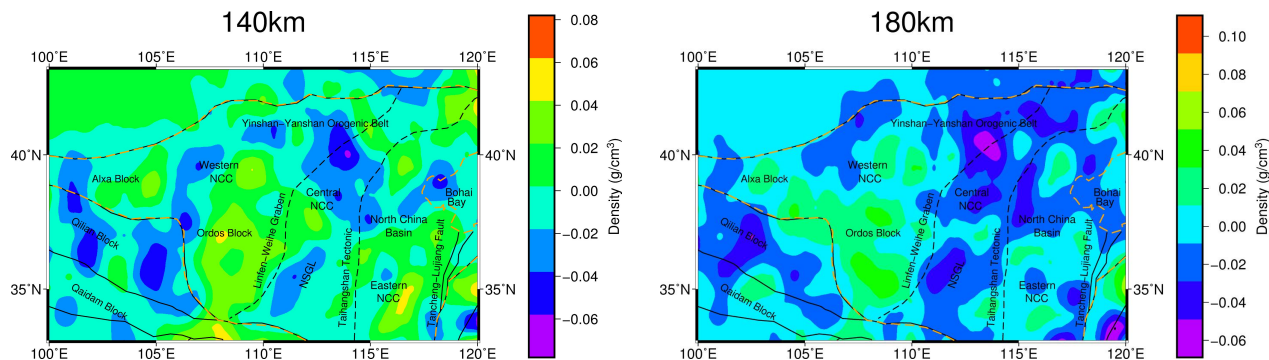
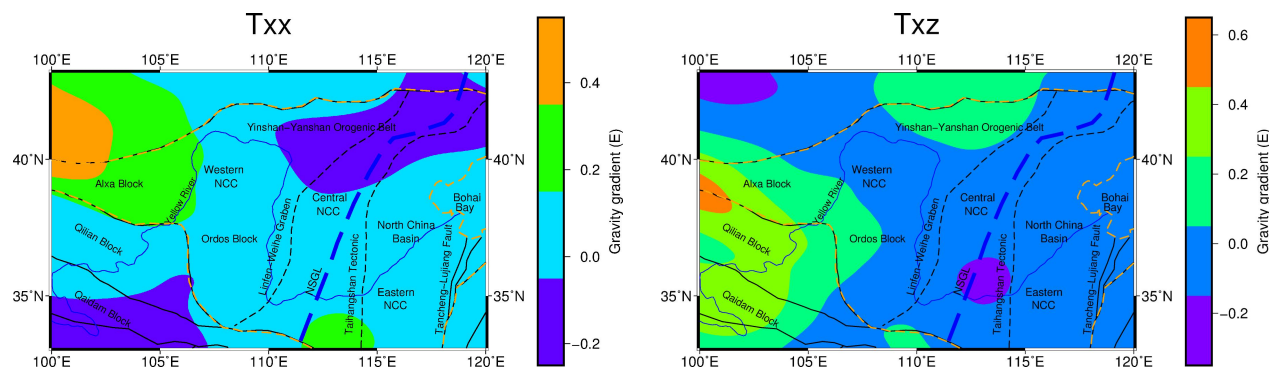


Figure 6 Lithospheric density distribution of NCC by gravity at different depths.

745 3.2 Obtain GOCE satellite data for study area

The GOCE L2 (GOCE GO_CONS_EGG_TRF_2) gravity gradient measurement product provided for users includes the gravity gradient data **along the orbit**. This study directly downloaded the preprocessed gravity gradient anomaly data with the spatial resolution of 10 arc-min, which was acquired over 48 months from November 2009 to October 2013 (Sebera et al., 2014), from the website GOCE+ Geoexplore II (<http://http://goce.kma.zcu.cz/data.php>). These data sets have undergone average orbit height correction (Sebera et al., 2014) and normal gravity gradient correction (Mortiz, 1980; Šprlák, 2012). The geographic area within E100°–E120° and N33°–N43° is defined as the study area (Fig. 7a–d), where the area of NCC is located.

750



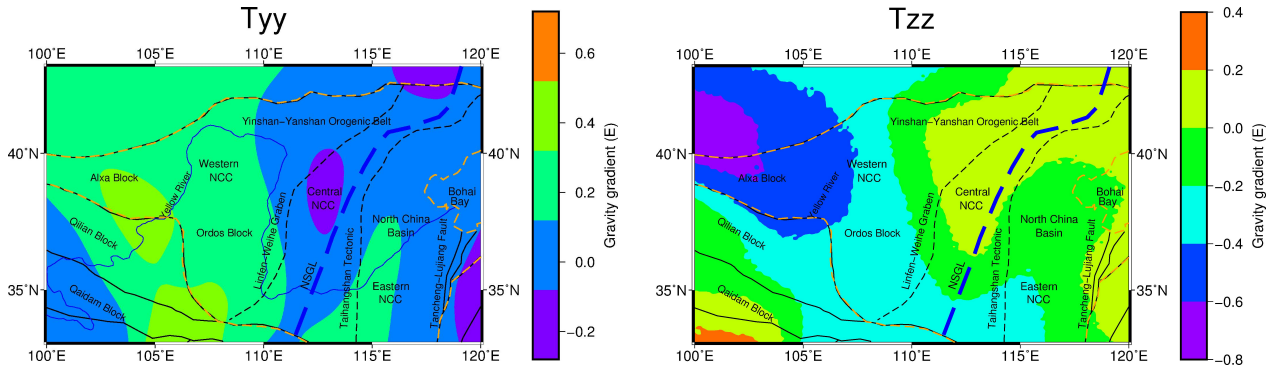
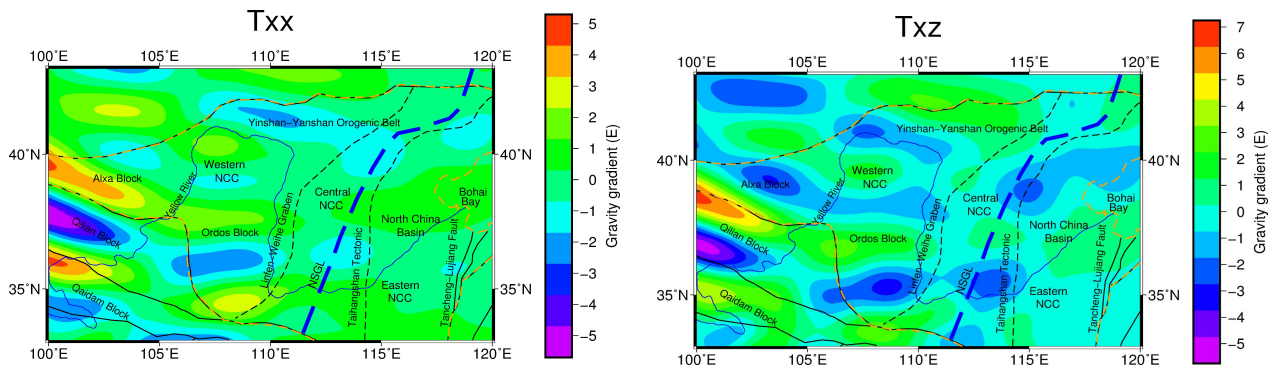


Figure 7 The gravity gradient anomaly (T_{xx} , T_{xz} , T_{yy} , T_{zz}) after average orbital correction to the altitude of 250km.

755 3.3 Downward continuation

The data of the GOCE satellite at the average orbit height only reflect the long wavelength information and the large structure features inside the earth. To highlight the high frequency information of the shallow anomaly body and detailed information of the structural features, such as depth and shape, the GOCE satellite data at the average orbit height for the NCC have been downward continued to the near surface area (Martinec, 2014). The obtained results benefit for the lithospheric structure analysis for local areas. The software Tesseroids developed by Uieda et al. (2016) is used in the calculation of the topography and the underground interface undulation effects. To ensure the accuracy of the calculation, the software recommends a distance of at least 1 km between the observation plane and the mass body, while the highest point of the topography in the study area is located at approximately 5 km. Thus, the gravity gradient components are downward continued to 10 km above the geoidal surface (Fig. 8a–d). The iterative continuation methods based on the Poisson approximate integration theory, specifically developed for satellite gravity gradient components by Sebera et al. (2014), are adopted, in which the space outside the earth surface is regarded to be mass free.



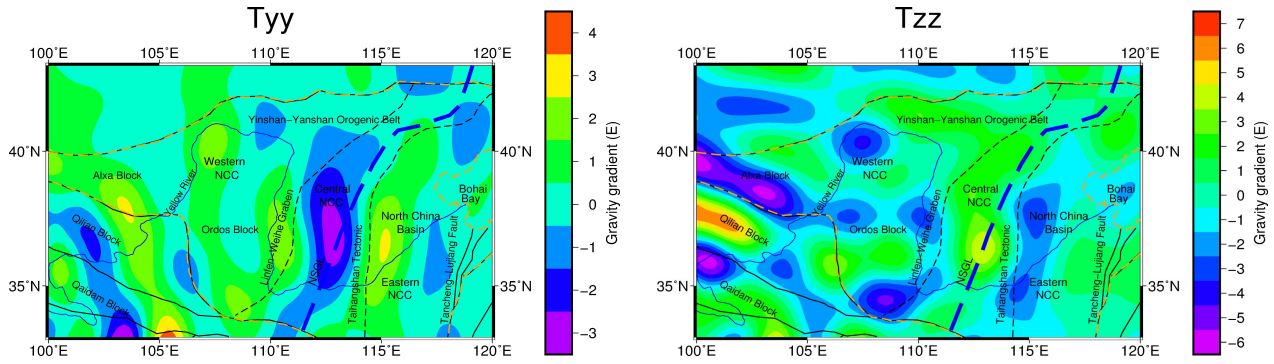


Figure 8 The gravity gradient effect (T_{xx} , T_{zz} , T_{yy} , T_{zz}) after downward continuation to the altitude of 10km .

3.4 Correction for the topographic effects

The gravity gradient anomaly components after downward continuation are a combination of the interface undulation and density heterogeneity. Thus, the topographic correction, underground interface undulation correction and long wavelength correction should be carried out in accordance with the existing precise models. **These three corrections are affected by the masses within and outside the study area, the far zone corrections outside the study area should be taken into consideration (Szwilius et al., 2016). Therefore, the correction radius in the study area is extended by 10° for all corrections. The extended geographic area within E90°–E130° and N23°–N53° is defined as the calculation area (Fig. 13 e-f). And the obtained results in the study area are cut out from the calculation area.**

First, the topography effects are calculated using the software Tesseroids (<https://tesseroids.readthedocs.io/en/latest>) developed by Uieda et al. (2016), which is aimed at **reducing** the gravity anomaly induced by the topographic mass above the geoidal surface from the gravity gradient after continuation. The software Tesseroids is able to convert the spherical hexahedron (tesseroid) in the spherical coordinate into the prism in the Cartesian coordinate to calculate the corresponding gravity gradient effects for topography. The software Tesseroids provides the built-in module to calculate the topography effects, for which the calculation is based on the topography elevation data ETOPO1 with the spatial resolution of 1' × 1' (Amante and Eakins 2009).

In order to directly reveal the correlation between the topography and the calculated gravity gradient effects, the three dimensional figure of topographic gravity gradient effect T_{zz} is shown in Fig. 9e, where the interface undulation represents the topography (Fig. 1), and the colour reflects the gravity gradient effects T_{zz} (Fig. 9d).

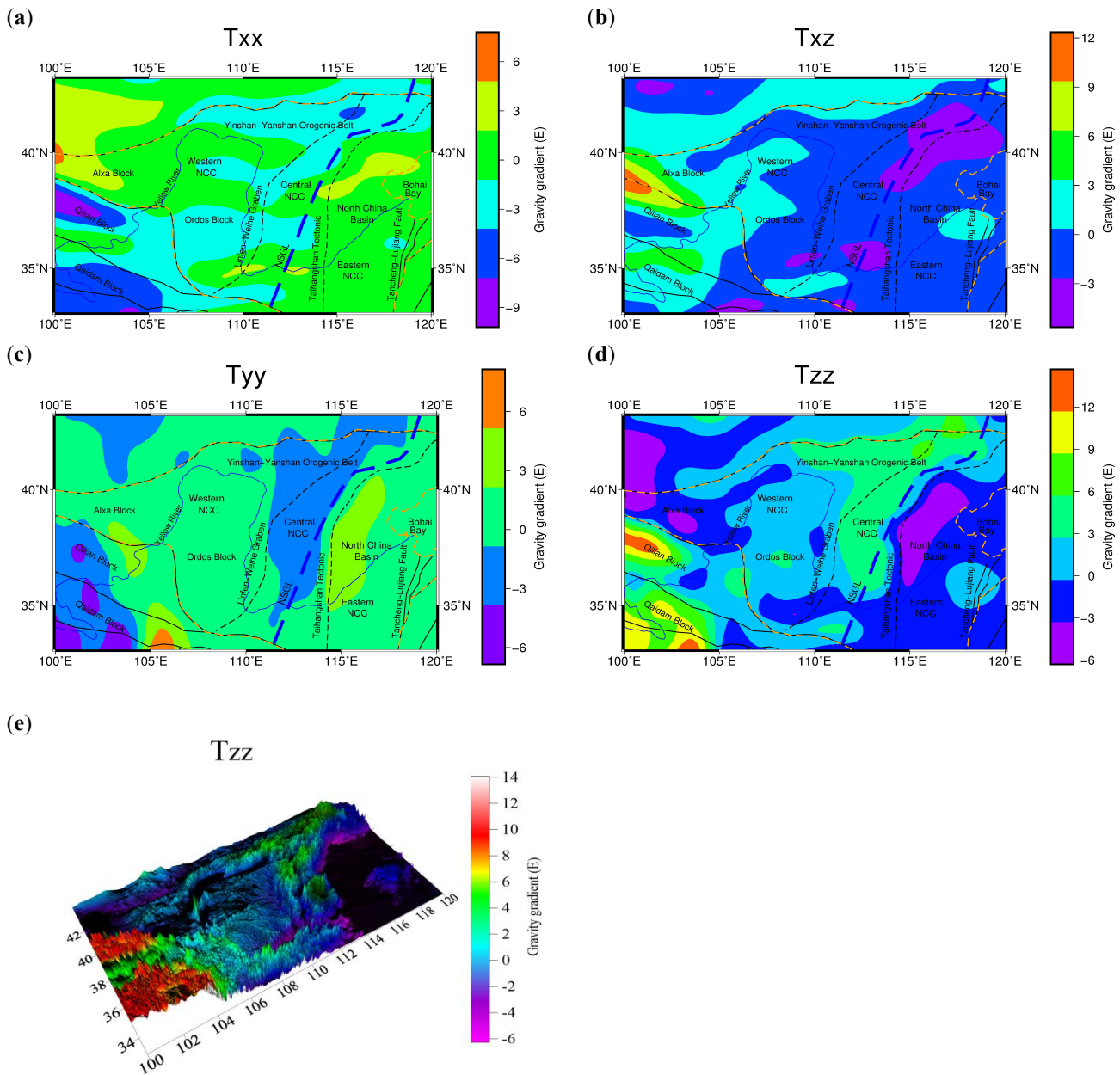


Figure 9 The gravity gradient effect caused by the topographic masses, (a) T_{xx} , (b) T_{xz} , (c) T_{yy} , (d) T_{zz} , (e) The 3D gravity gradient effect T_{zz} of topography.

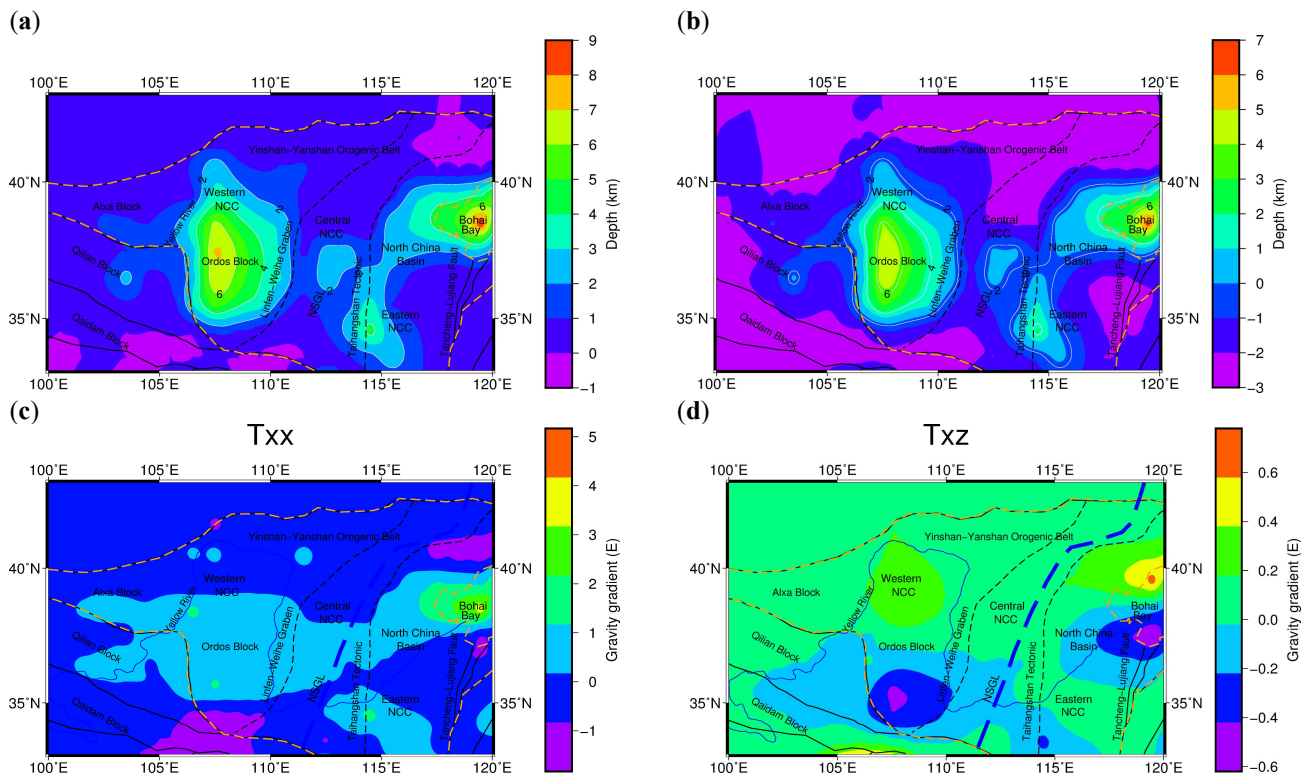
790 3.5 Correction for the underground interface undulation effects

First, the average depth and density of the sediment in this area should be calculated for the interface undulation effects. The average depth is calculated from the depth data of the sediment in NCC (Fig. 10a) provided by CRUST 1.0 with the spatial

795 resolution of $1^\circ \times 1^\circ$ (Laske et al., 2013), and then the interface undulation data of the sedimentary layer (Fig. 10b) are
 obtained after correcting for the average sedimentary layer depth. With respect to the calculated average depth, all the
 density data corresponding to the average depth are extracted in order to calculate the average density corresponding to the
 average sedimentary layer depth. The average sedimentary layer depth in NCC is calculated to be 2.3 km, and the
 corresponding average density is 2.45 g/cm^3 . Based on CRUST 1.0, the actual depth and density are adopted instead of
 empirical value. Moreover, the differences in the actual depth and density at each point from the average depth and density
 are calculated using the tesseroïd forward modelling method based on the software Tesseroids. Consequently, the gravity
 800 gradient effects induced by the sedimentary layer undulation in NCC are obtained (Fig. 10c–f).

To more intuitively illustrate the correlation between the sedimentary layer interface undulation and the calculated gravity
 gradient effects, in Fig. 10g, the interface undulation denotes the sedimentary layer interface undulation (Fig. 10b), and the
 contour lines represent the corresponding gravity gradient effects T_{zz} (Fig. 10f).

805



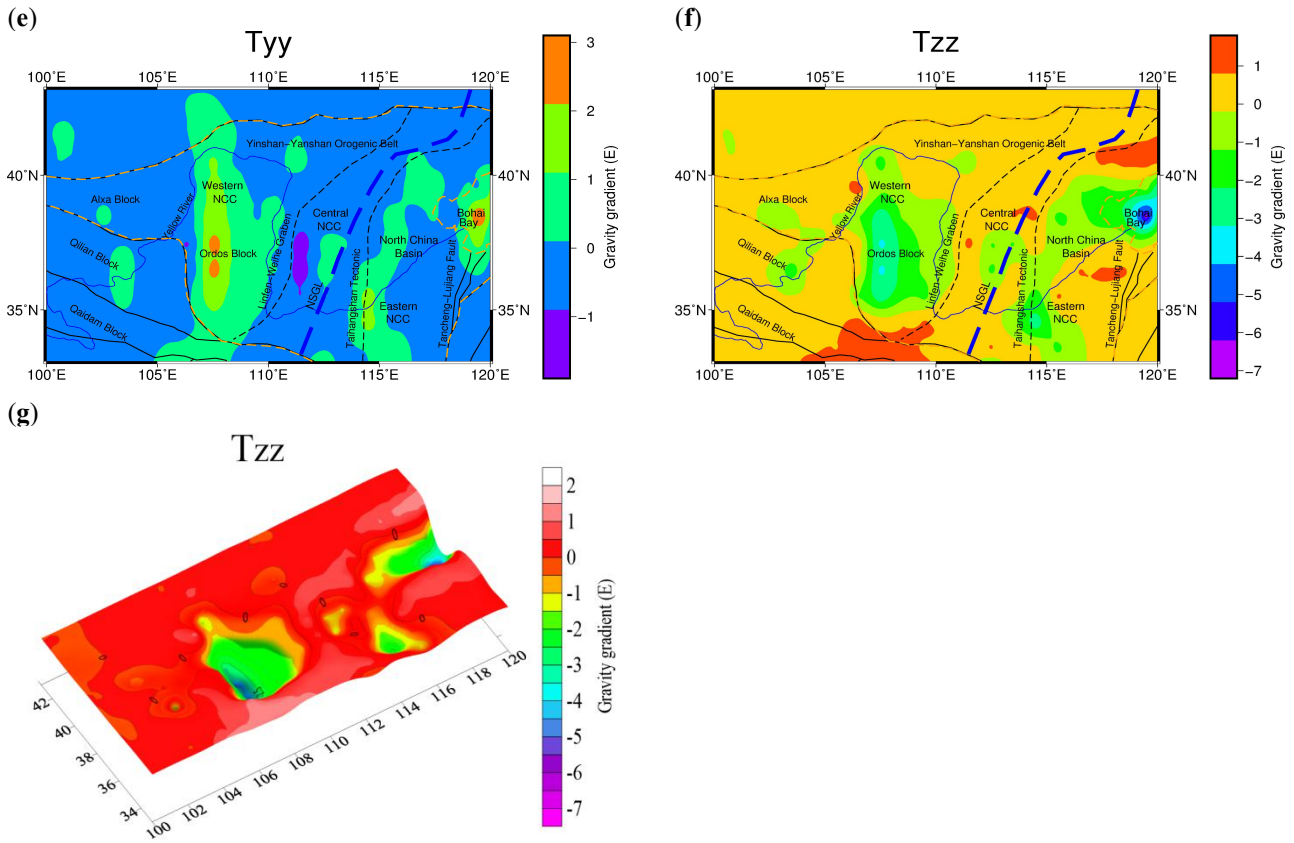
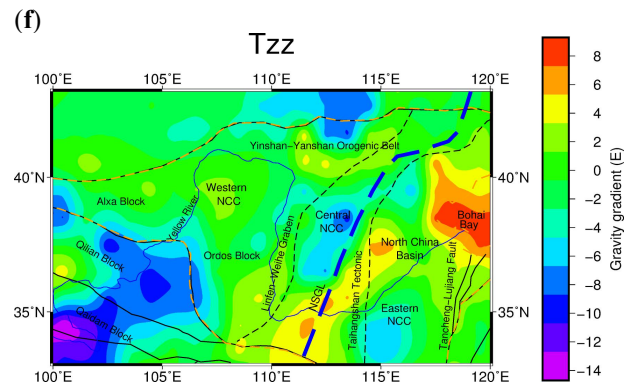
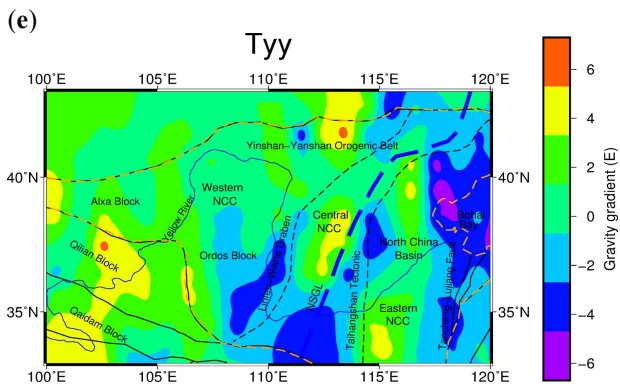
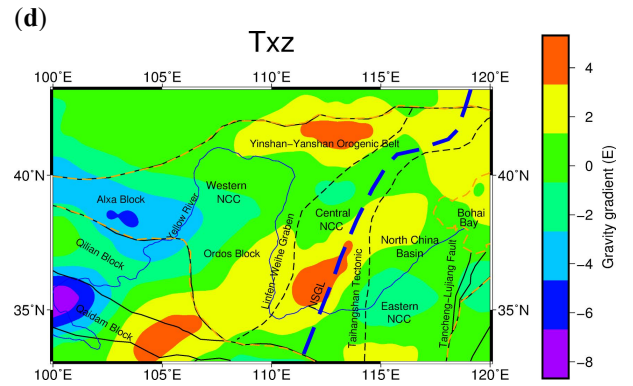
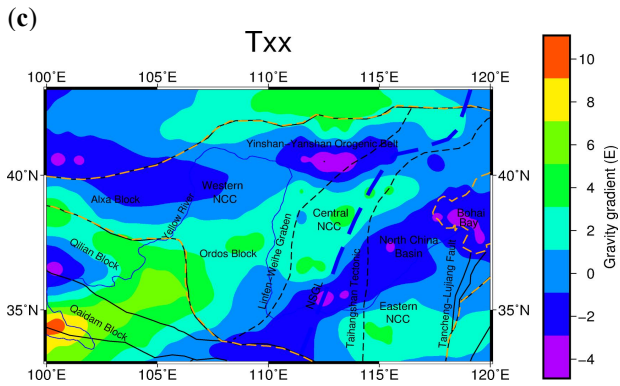
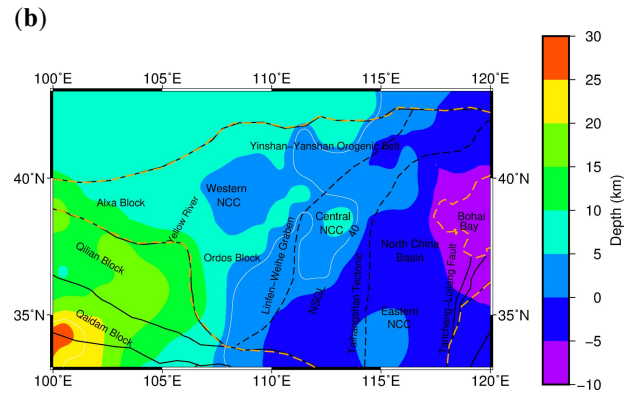
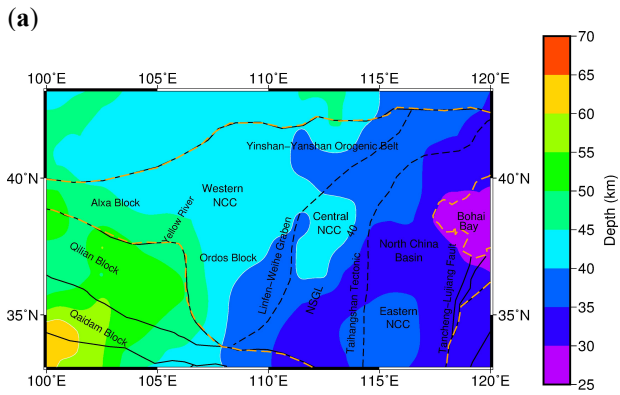


Figure 10 (a) Sedimentary layer interface of the NCC. (b) Sedimentary layer interface undulation of the NCC. The anomalous gravity gradient component caused by the relief at the sedimentary layer interface undulation, (c) T_{xx} , (d) T_{xz} , (e) T_{yy} , (f) T_{zz} . (g) The 3D gravity gradient effect T_{zz} of sedimentary layer interface undulation.

810 The depth of the Moho interface in NCC provided by CRUST 1.0 is shown in Fig. 11a. The average depth calculated from the depth data of the Moho is 36.5 km, and the corresponding average density is 3.32 g/cm³. The Moho undulation after correction for the average depth is illustrated in Fig. 11b. Similarly, the gravity gradient effects induced by the Moho undulation can be calculated. The gravity gradient effects induced by the Moho interface undulation based on the Tesseroids software are presented in Fig. 11c–f. And the three dimensional gravity gradient effect T_{zz} induced by the Moho interface

815 undulation is shown in Fig. 11g, where the interface undulation reflects the Moho undulation (Fig. 11b) and the contour line represents the gravity gradient effects (Fig. 11f).



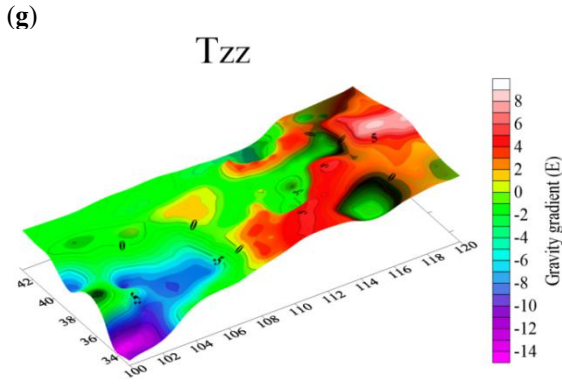


Figure 11 (a) Moho interface of the NCC. (b) Moho interface undulation of the NCC. (c) The anomalous gravity gradient effect caused by the Moho interface undulation. (c) T_{xx} , (d) T_{xz} , (e) T_{yy} , (f) T_{zz} . (g) The 3D gravity gradient effect T_{zz} of Moho interface undulation.

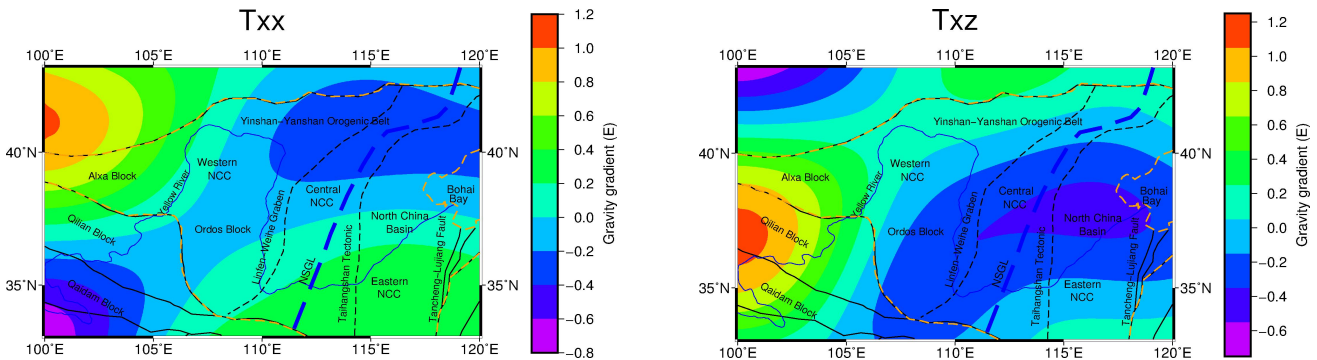
820 3.6 Correction for the gravity gradient effects of the mantle under 180km

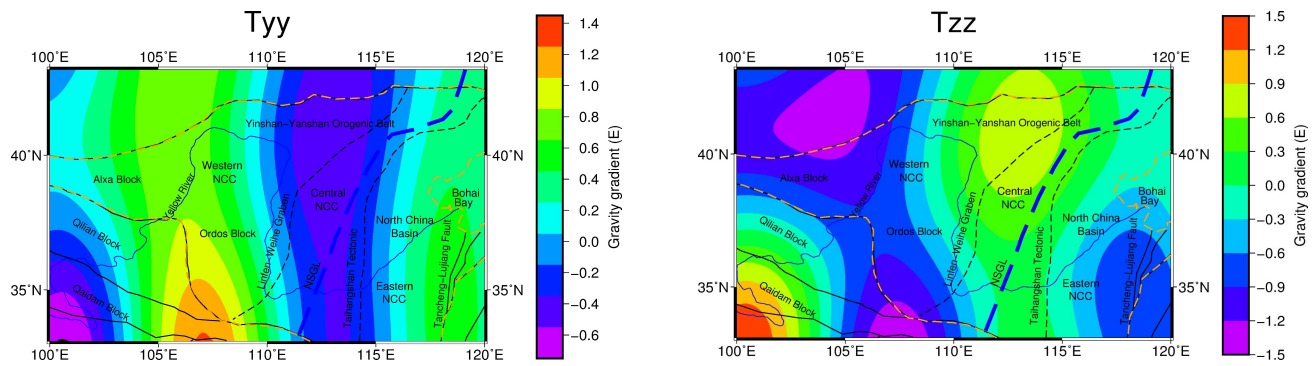
The long wavelength gravity gradient effects are mainly induced by substance density heterogeneity in the lithosphere at depths deeper than 180 km. The correlation between the depth of the field source and the order of the spherical harmonic function of the gravity potential developed by Bowin et al. (1986) is adopted:

$$Z=R/(n-1) \quad (17)$$

825 where Z is the depth of the field source; R is the radius of the Earth; and n is the order of the spherical harmonic function.

The long wavelength gravity gradient anomalies effects corresponding to the 2nd–33th order spherical harmonic coefficients (Wang et al., 2014) in the EGM2008 are calculated. **The gravity gradient effects induced by the long wavelength are presented in Fig. 12.**





830 **Figure 12** The gravity gradient effect (T_{xx} , T_{xz} , T_{yy} , T_{zz}) caused by the lithosphere under 180km.

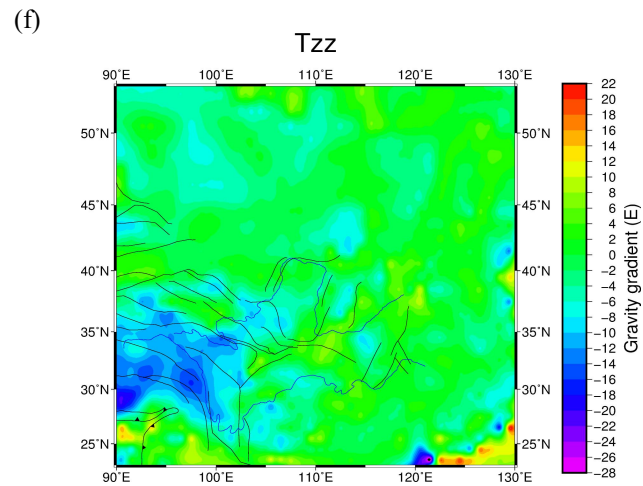
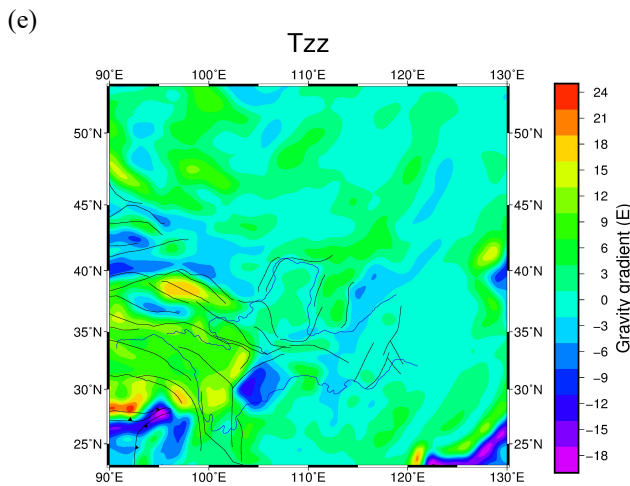
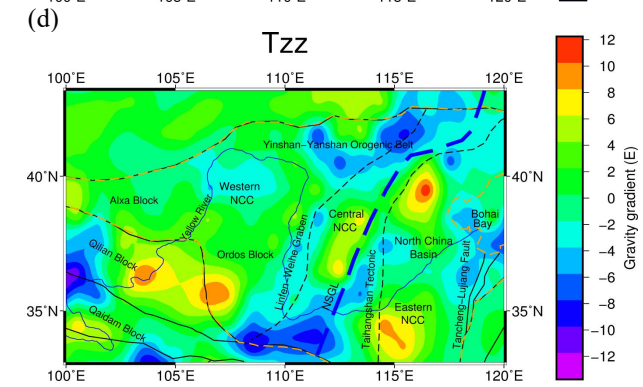
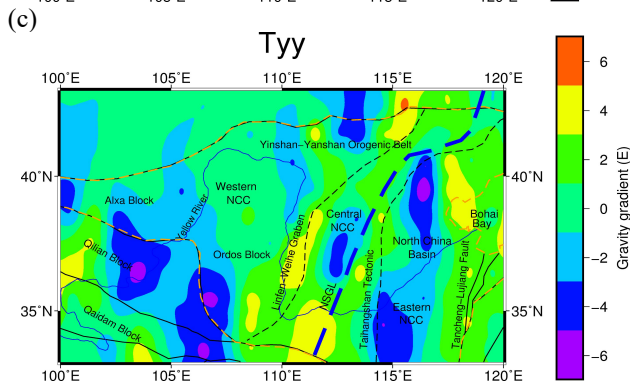
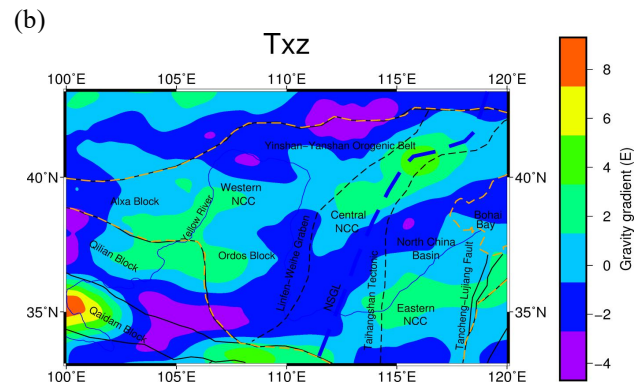
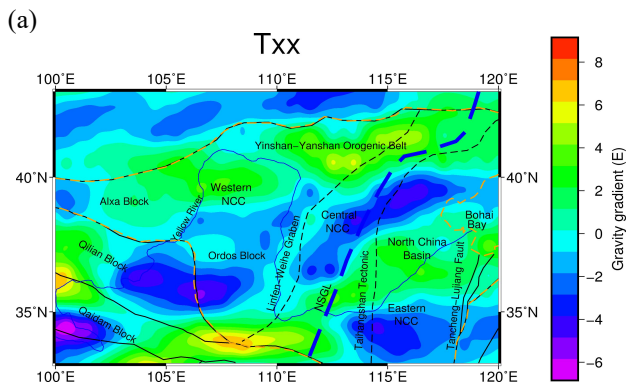
3.7 The corrected gravity gradient components

Since models with different spatial resolution are used in several corrections, the spatial resolutions of the obtained results are different. Therefore, before calculating the corrected gravity gradient component, the resolutions of the results for each calculation are homogenized the same spatial resolution of $0.5^\circ \times 0.5^\circ$. For the higher spatial resolution of the data (e.g. gravity gradient data after downward continuation, topographic correction), we extracted data from the calculated results. For the gravity gradient correction caused by the underground interface undulation, the common kriging interpolation method was adopted to obtain the data needed for the spatial resolution. The corrected gravity gradient anomaly components (Fig. 13) are obtained after deducting topography effects, the underground interface undulation effects and the long wavelength effects from the gravity gradient tensor data after downward continuation.

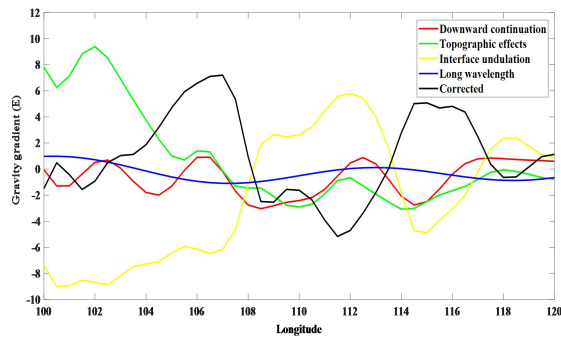
840

The amplitude of the topography effects and the underground interface undulation effects is obvious, but topographic correction and underground interface undulation correction balance each other out to a certain degree (Szwilius et al., 2016). This counteraction can be obviously found with the extended study area in Fig. 13e (Topographic correction) and Fig. 13f (Underground interface undulation correction). The detailed statistics amplitude for each gravity gradient correction are summarized in Table 3. For better presenting different corrections intuitively, several corrections T_{zz} at different cross sections latitude 35° and latitude 37.5° are presented in Fig.13 (g-h).

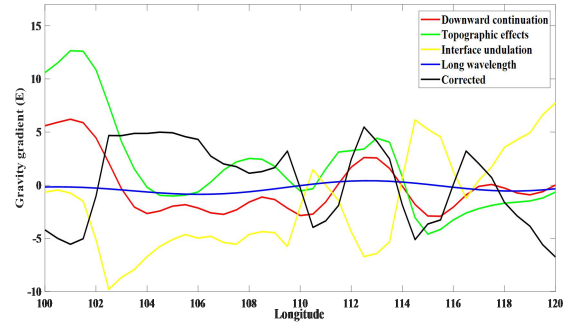
850



(g)



(h)



855 **Figure 13** The corrected gravity gradient components (a) T_{xx} , (b) T_{xz} , (c) T_{yy} , (d) T_{zz} . Gravity gradient effects with extended area (e) Topographic effects T_{zz} , (f) Interface undulation T_{zz} (Sedimentary and Moho) effects. Several corrections T_{zz} at different cross sections (g) Latitude 35° , (h) Latitude 37.5° .

860

Table 3 Statistics for each gravity gradient correction.

| Gravity Gradient Effects (E) | Downward Continuation Maximum (E) | Downward Continuation Minimum (E) | Topographic Effects Maximum (E) | Topographic Effects Minimum (E) | Interface Undulation Effects Maximum (E) | Interface Undulation Effects Minimum (E) |
|------------------------------|-------------------------------------|-------------------------------------|---------------------------------|---------------------------------|--|--|
| T_{xx} | 5.3 | -5.7 | 6.3 | -9.4 | 10.1 | -4.9 |
| T_{xz} | 7.2 | -5.6 | 11.9 | -5.6 | 5.2 | -8.9 |
| T_{yy} | 4.8 | -3.6 | 7.2 | -6.8 | 6.3 | -6.7 |
| T_{zz} | 7.5 | -6.5 | 13.8 | -6.3 | 7.7 | -14.1 |
| Gravity Gradient Effects (E) | Long Wavelength Effects Maximum (E) | Long Wavelength Effects Minimum (E) | Corrected Effects Maximum (E) | Corrected Effects Minimum (E) | | |
| T_{xx} | 1.1 | -0.8 | 8.7 | -6.8 | | |
| T_{xz} | 1.2 | -0.7 | 8.5 | -4.7 | | |
| T_{yy} | 1.4 | -0.7 | 6.7 | -6.6 | | |
| T_{zz} | 1.5 | -1.5 | 11.5 | -12.3 | | |

875

4 Results

In Fig. 14, after 8 iterations, the curve of defined RMS misfit tends to be horizontal, the variation is more and more slight between the values of defined RMS misfit, an calculated RMS misfit of 9.0×10^{-3} was obtained, at which point the inverse iterative computation was complete. As shown in the inversion results (Fig. 15), an obvious heterogeneity is present in both the horizontal and vertical distributions of the lithospheric density within the NCC, and it is specifically featured by a

880

segmented spatial distribution of the lithospheric density. In comparison (Fig. 6), inversion based on the gravity gradient provides more local and detailed information about the density anomaly distribution within the entire NCC. The maximum and minimum value of inversion results based on the gravity gradient has larger range, the detailed data statistics is summarized in Table 4. The center of anomalies are more concentrated with regional anomaly features, which is more favourable for the discussion about the stability and destruction in different regions of the whole NCC area. In the eastern NCC, the boundary of density differences on both sides of Tancheng-Lujiang fault belt zone are more obvious; the extreme value of low density anomalies present continuously in Bohai Bay area at the depth of 60km-80km. In the central NCC, it is easier to determine the centre of density anomaly distribution in the southern, middle and northern part of Taihang Orogenic belt at 42km-80km, which has different regional block features of density anomaly. In the western NCC, the results of gravity inversion is connected as a whole, however, the result of gravity gradient inversion shows the Southeast trend of Qilian block, which is more favorable for the geodynamic analysis in the western NCC.

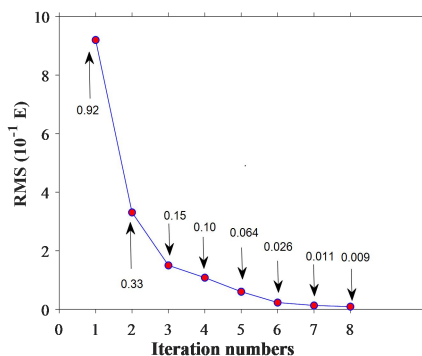


Figure 14 With the iterative calculation, residual mean square between the forward calculated theoretical gravity gradient and the gravity gradient measurements versus iteration number in the PCG inversion algorithm.

Table 4 Comparison of gravity and gravity gradient inversion results.

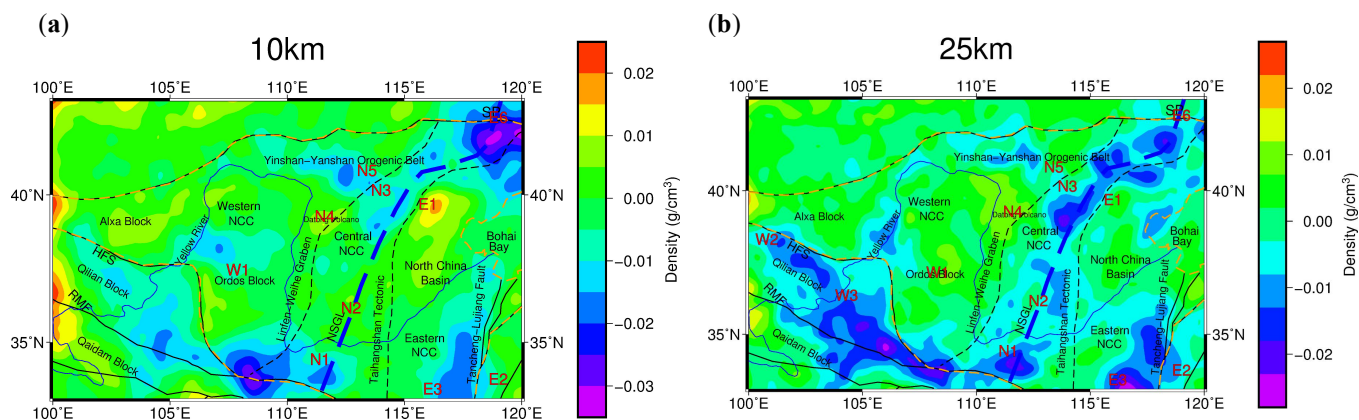
| Depth Inversion Results | 10km (g/cm ³) | 25km (g/cm ³) | 42km (g/cm ³) | 60km (g/cm ³) | 80km (g/cm ³) | 100km (g/cm ³) | 140km (g/cm ³) | 180km (g/cm ³) |
|---------------------------------------|--------------------------------------|------------------------------|------------------------------|------------------------------|------------------------------|-------------------------------|-------------------------------|-------------------------------|
| | Maximum density of gravity inversion | 0.023 | 0.021 | 0.011 | 0.035 | 0.053 | 0.056 | 0.058 |
| Maximum density of gradient inversion | 0.025 | 0.026 | 0.015 | 0.043 | 0.058 | 0.070 | 0.077 | 0.091 |
| Minimum density of gravity inversion | -0.033 | -0.026 | -0.022 | -0.020 | -0.024 | -0.061 | -0.066 | -0.064 |
| Minimum density of gradient inversion | -0.035 | -0.028 | -0.025 | -0.023 | -0.028 | -0.063 | -0.078 | -0.069 |

900 **5 Discussion**

In general, obvious density anomalies at a depth of 10 km are only seen in the eastern and central areas of the NCC. At the depth of 25-40 km, significant negative density residuals are present in the Taihang Orogenic belt along the central NCC, also the Qilian and Qaidam blocks along the western NCC. The significant high density residuals exist in the Ordos block. For the depth of 60-80 km, low density residuals are found in the Bohai Bay area in the eastern NCC, while widely distributed low density residuals are seen in the Yinshan Orogenic belt. At a depth of 100 km, the entire NCC is characterized by spatially alternating positive and negative density residuals. In comparison, at the depth of 140-180 km, an obvious regional differentiation in the density anomaly distribution is seen, obvious low density residuals in the Datong volcano at the junction of the Yinshan-Yanshan Orogenic and the Taihang Orogenic belt in the eastern NCC, as well as the Qilian block at the junction of the Qaidam and Ordos blocks in the western NCC.

910 According to the horizontal spatial distribution of the lithospheric density, the NCC is divided into three main areas, namely, the eastern NCC, consists of the North China Basin and the Bohai Bay area; the central NCC, consists of the central transitional belts; and the western NCC, consists of the Ordos Basin and its surrounding areas. **Based on three main local density anomalies areas in Fig. 15a-h, the density anomaly distribution in each area at different depths are discussed.**

915



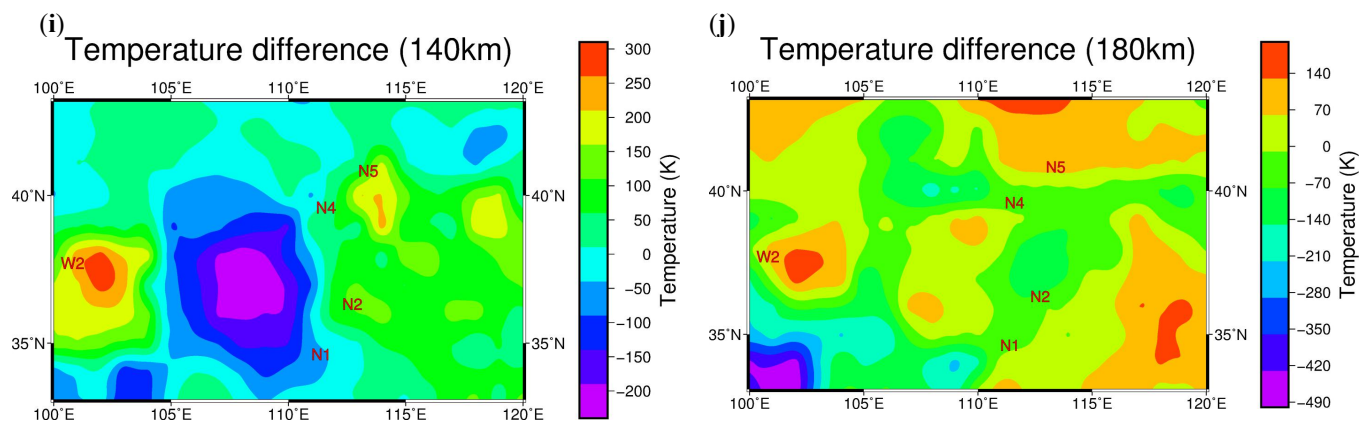


Figure 15 Lithospheric density distribution of NCC at different depths, (a) 10 km , (b) 25 km , (c) 42 km , (d) 60 km , (e) 80 km , (f) 100 km , (g) 140 km , (h) 180 km . Temperature difference at (i) 140 km , (j) 180 km . E represents eastern NCC, N represents central NCC, W represents western NCC; HFS Haiyuan fault system, RMF Riyue mountain fault, SP Songliao plain .

920

5.1 Eastern NCC

The eastern NCC is characterized by obvious features with connections to the Bohai Bay. In the eastern NCC, the distribution of positive and negative densities is always characterized alternately within the depth 0-180km. From the Tancheng-Lujiang fault belt (E2 and E3) in the south, Bohai Bay (E5) and North China Basin (E1) in the middle, to the Songliao Basin (E6) in the north, the density always has the features of regional distribution instead of large-scale distribution in the central NCC. The obvious spatial distributions of the density anomalies are consistent with the theory that this area has experienced strong deformation (Tian and Zhao, 2011).

At the depth interval of 10-180 km in the eastern NCC, there are positive density anomalies in the E1 area of the North China Basin, which are mainly distributed along the Tangshan-Xingtai earthquake belt. The result is consistent with the positive P-wave velocity along the earthquake belt (Huang and Zhao, 2004; 2009), which implies the positive density distribution affected by the Tangshan-Xingtai earthquake belt.

The Tancheng-Lujiang fault belt is one of major North-Northeast fault zones in the East Asia continent. This fault belt extends more than 2400 km in China, which cuts through different structural units (Huang et al., 2011). The geological structure of the Tancheng-Lujiang fault belt is complicated. Along the Tancheng-Lujiang fault belt in the eastern NCC is extended in the North-Northeast direction, on both sides of which (the E2 area in the right and the E3 area in the left) density anomalies are significantly different. At a depth of 42 km, significant positive density residuals are present in the E3 area as the locally extreme value, while regional positive density residuals are observed in the E2 area (Fig. 15c). At a depth of 80 km, significant positive density residuals are present in the E3 area, while no density anomalies are observed in the E2 area

940

(Fig. 15e). At a depth of 100-180 km, the density anomalies are obvious (Fig. 15h), including those in the E3 area with a direction consistent with the fault belt strike and those in the E2 area with alternating distributions of positive and negative density residuals. Moreover, these positive and negative density residuals are the local extremes, reaching 0.10 g/cm^3 and -0.06 g/cm^3 , respectively. On both sides of the Tancheng-Lujiang fault belt, there are no large-scale density anomalies connected with each other exist, the density anomalies distribute along the Tancheng-Lujiang fault belt with different features. This distribution represents density differences between different tectonics units. Therefore, the Tancheng-Lujiang fault belt is obvious as the boundary of the tectonics units. In addition, based on the study of seismic receiver functions (Chen et al., 2006; Li et al., 2011), the Tancheng-Lujiang fault belt zone and its extension are the most obvious areas of lithospheric thinning in the eastern NCC, the thickness of the lithosphere is just 60-70km. The significant different density distribution on both sides of the Tancheng-Lujiang fault belt, which indicates the fault belt may have penetrated the lithosphere.

In the E5 area of the Bohai Bay, there are significant negative density anomalies at the depth of 60-80 km. This area is featured by the columnar shape density distribution at a depth of 80 km. However, with the depth increasing from 100 km to 180 km, there are no continuous regional negative density residuals in the E5 area. In contrast, distinct low density residuals are seen in the E4 area, which is in the extended region of the Tancheng-Lujiang fault belt. Meanwhile, density anomalies are seen in the extended region of the major fault belt in the adjacent area of the eastern boundary of the Tancheng-Lujiang fault belt. According to previous studies (Teng et al., 1997; Su et al., 2009), these density anomalies are ascribed to the extension of the Tancheng-Lujiang fault belt and the development of the mantle plume in the deep Bohai Bay area. But the distribution of density anomalies in this region does not conform to the features of the mantle plume with continuous negative density residuals in the mantle. Based on this study, these density anomalies are mainly ascribed to the extension of the Tancheng-Lujiang fault belt. The negative density residuals (E4) exists at the extension of the Tancheng-Lujiang fault belt continuously (100-180km), which implies the region at the extension of the fault zone has been penetrated the crust to the mantle. The cutting effect of the Tancheng-Lujiang fault belt and the lithospheric thinning (Chen et al., 2006; Li et al., 2011) result in asthenosphere upwelling with negative density residuals in Bohai Bay.

In the E6 area, which is a transitional area between the Yanshan block and the Songliao Basin, significant low density residuals are present at a depth of 10 km (Fig. 15a). As the depth increases, persistent high density residuals are seen in the upper mantle, especially at the depth range of 100-140 km, with the value reaching up to $0.07\text{-}0.08 \text{ g/cm}^3$. Moreover, the density anomalies are aligned in the southwest direction at depths of 140-180 km relative to those at depths of 0-100 km. This phenomenon is attributed to the southwest extension of the high density mantle lithosphere below the Songliao Basin, reaching the region below the Yanshan Orogenic belt.

5.2 Central NCC

The central NCC, formed by the central transitional zone, is characterized by significant low density residuals with obvious segmented distributions. The Taihang Orogenic belt is generally Northeast-Southwest oriented, and it can be divided into three blocks, namely, the southern block N1, the middle block N2, and the northern block N3. From 42 km to 100 km, N1 is connected to the high density anomaly area of the western NCC (W4), while N3 is connected to the high density anomaly area of the eastern NCC (E1), and low density anomaly area in the Yinshan-Yanshan blocks (N5). Blocks N3 and N5 are connected with each other forming low density anomaly in large scale area. These features may indicate the that Taihang Orogenic belt have experienced different geological processes from south to north.

N4 in the northern part of the Linfen-Weihe Graben block is mainly distributed in the Datong volcanic area. As the depth increases, the density anomalies significantly become high density residuals at 25 km (Fig. 15b), and then becoming obvious low density residuals from 42 km to 140 km. Although the Datong volcano is no longer active (Tian et al., 2009), its surrounding area still exhibits low density residuals. Similarly, N5 at the junction of Yinshan-Yanshan and the north of the Taihang Orogenic belt, where is featured by obvious low density residuals at depths of 60-180 km. When the depth increases to 60 km (Fig. 15d), these anomalies become connected with N3 in the north of the Taihang Orogenic belt and with N4 at the junction of the Datong volcanic area, forming a large low density anomaly zone. As the depth further increases, the low density anomaly area covering N5 presents persistently negative density residuals that extend down to a depth of 180 km (Fig. 15h). Moreover, the negative density anomaly value is more significant.

From the distribution of temperature difference (An and Shi, 2007; Yang et al. 2013) in Fig 15 i-j, the N5 is located at the area with continuous high heat environment. Based on previous studies by magnetotelluric imaging method (Zhang et al., 2016), melting occurs at the mantle of Datong volcanic area and north of the Taihang Orogenic belt. According to the seismic receiver function, the Poisson's ratio in the north of Taihang Orogenic belt is as high as 0.3, while in the south of Taihang Orogenic belt is just about 0.25-0.26 (Ge et al., 2011). The Poisson's ratio of continent is generally between 0.25-0.27, although the temperature and material composition seem to have a dominant influence on Poisson's ratio (Zandt and Ammon, 1995), it is difficult to increase the Poisson's ratio to 0.3 only by the change of material composition. Therefore, the obvious negative density residuals in this area is mainly affected by the high heat environment. The upwelling of the thermal materials from deep asthenosphere formed the magma migration pathway, which transforms the lithosphere and the upper mantle apparently.

In contrast with north regions (N3 and N5), negative density residuals is observed at the central (N2) and southern part (N1) of Taihang Orogenic belt from 60km to 180km, with the extreme value -0.048g/cm^3 at a depth of 180km. But at the depth of mantle, the central south part does not show the features with high continuous heat environment. At a depth of 140km, the

temperature at southern block of Taihang Orogenic is lower than the average temperature, the temperature is higher than the average temperature only at middle block of Taihang Orogenic. With the depth increases, the temperature at southern and middle block of Taihang Orogenic all lower than the average temperature at the depth of 180km. And the Poisson's ratio of this area accords with the typical continental features. The thermal erosion is always accompanied by the high heat flow environment, which is not consistent with this feature in the central and southern region of Taihang Orogenic belt. Therefore, it is inferred that the impact of temperature is limited, the obvious negative density anomalies may be caused by the delamination.

N6 in the central NCC exhibits significant positive density residuals at the depth of 140-180km, which contrast the low density residuals over a large area of the central NCC. The mantle part of N6 is connected to the positive density anomaly area in the W1 area, Ordos block, western NCC (Fig. 15e-f). While in Fig. 15i-j, the temperature in N6 is normal at the depth of 140-180km, and the temperature boundary exists between N6 and W1 areas. Based on previous studies (Ai et al., 2019), Taihang Orogenic belt in the mantle part experiences the blocking effect by the rigid Ordos block during expansion of the orogenic belt. And the stable Ordos block area presents continuous large scale high density residuals. It is inferred that the Ordos block blocking effect makes the positive density residuals exist in central NCC (N6) and connect with the Ordos block.

5.3 Western NCC

Strong tectonic deformation and significant magmatic activities since the Mesozoic and Cenozoic have resulted in the complex tectonic patterns in the Ordos block and its surrounding areas (Zhang et al., 2011). The Ordos block is surrounded by the Yinchuan-Hetao and Shaanxi-Shanxi rift valleys, and it is overall a stable tectonic unit.

At a depth of 42 km, the W1 area in the central Ordos block is characterized by high density residuals (Fig. 15c), whereas no obvious anomalies are seen in the northern part of the Ordos block. According to the receiver function (Tian and Zhao, 2011), the central part of the Ordos block is 41 km thick, which thickens to 45 km in the northern part. Therefore, it can be inferred that the southern part of the Ordos block has entered the lithospheric mantle at a depth of 42 km. From 60 km to 100 km, the high density residuals in the W1 area of the central Ordos block gradually change to low density residuals. At the depth interval of 140-180 km, the high density residuals still dominate the W1 area of the central Ordos block. Although Ordos is a relatively stable block with high density features, the low density blocks invasion appears at 80-100km depths. At a depth of 80 km, the low density anomaly of Ordos block (W1) at east side is connected with the low density anomaly at central NCC (N2), which indicates that Ordos is affected to some extent by the destruction of the central NCC. At a depth of 100km, the low density anomaly of Ordos block (W1) is connected with Qilian block (W3) and Qaidam block (W5), the distributions of

the density anomalies are consistent with the theories that Ordos block is affected by the northeast compression of the Qinghai-Tibet Plateau and deep substantial expansion (Sheng et al., 2015).

1040

The whole Qilian block (W2 and W3 areas) is featured by significant low density residuals in the crustal part at 25-40 km, which falls in the range of the Haiyuan fault belt. The boundary of the negative density residuals is essentially consistent with the strike of the fault belt shown on the surface. The W3 area at the junction of the Qilian and Ordos blocks is characterized by a sharp transition from low density to significant high density. At the depth of 25-80 km, the density anomalies in the Qilian block present a dominant NW-SE strike; however, this strike turns clockwise to the NS direction as the depth further increases to 180 km, especially after entering the mantle. This observation is consistent with previous research results in this region. The mantle convective stress field calculated based on gravity anomalies is demonstrated to be significantly inconsistent with the crustal movement pattern (Xiong and Teng, 2002; Wang et al., 2013), which indicates obvious decoupling between the crustal and mantle materials in the Qilian block. The Qilian block is located at the junction of the north-eastern Qinghai-Tibet plateau and the Alashan and Ordos blocks in the western NCC. The Qilian block has not only been influenced by a collision and subduction of the Indian plate, but also by the blocking effect of the Ordos Block, which resulting in the strong regional tectonic stress background in the deep part of the Qilian block with an associated clockwise rotation of the material movement.

1045

1050

1055

As the depth increases in the range of 140-180 km, persistent obvious negative density residuals are increasingly dominant in the Qilian block (W2 areas) in the western NCC. According to the previous study (Teng et al., 2010), the lithosphere in the western NCC is the thickest, with an average depth of 140-150 km. However, within this depth range, the obvious low density residuals are present in the orogenic belts of the western NCC, which eliminates the possibility that the lithospheric thinning is the main cause of the density anomalies at the depth of 140-180 km. According to the temperature differences (Figure 15 i-j), Qilian block in the western NCC has a high temperature at the depth of 140km -180km. Furthermore, according to previous study on the terrestrial heat flux (An and Shi, 2007), the Qilian block has an average heat flux value up to 68.340 mW/m². Therefore, it can be concluded that the high heat flux environments lead to negative density residuals in the Qilian Block in the western NCC, accompanied by an upwelling of deep asthenosphere materials and the subsequent transformation of the mantle above the lithosphere.

1060

1065

5.4 The destruction mechanism of NCC

The low density anomalies in the Qilian Block and northern Taihang Orogenic belt are affected by the high heat flux environments. The low density anomalies in central Taihang Orogenic belt exist but not accompanied by the continuous high heat flux environments at mantle depth. However, without mantle plume found, the low density anomalies in the Bohai Bay are affected by the extension of the Tancheng-Lujiang fault belt, the mechanical extension makes the lithosphere destruction

1070

in this area. Based on our studies, one theory is hard to explain the destruction phenomena and modes in the whole NCC. The destruction of NCC is not only affected by the physical tension, but also caused by the thermal erosion and delamination. The former dynamic studies show that (Zhu et al., 2012; Zhu, 2018), since Mesozoic, the Pacific plate subducted westward to the Taihang Orogenic belt in the central part of the NCC. The residual dehydration of subducted plate in the mantle transition zone promoted the increase of the molten fluids content in the upper mantle beneath the NCC. The delamination and thermal erosion of the lithosphere in NCC just reflect different forms of mantle convection instability. Therefore, through this study, it is believed that the destruction in NCC is caused by several forms. The several destruction modes of the NCC coexist with different background of geological structures.

1075

1080

6 Conclusions

The sequential inversion of the lithosphere density structure in the NCC are divided into two stages. The effects of the initial density model are taken into consideration. The inversion results obtained by the inversion of corrected gravity anomaly are used as the initial model for the inversion of the GOCE satellite gravity gradient components. The GOCE satellite gravity gradient data were processed with several corrections to obtain the corrected gravity gradient components. The density distribution with the depth range of 0-180km in NCC shows that: (1) In eastern NCC, affected by lithosphere thinning, the eastern NCC is seen with local features in the density anomaly distribution. Obvious differences in the density anomaly distribution are observed, and the Tancheng-Lujiang fault belt in the eastern NCC penetrates through the lithosphere. The density anomaly in the Bohai Bay is mainly induced by the extension of the Tancheng-Lujiang major fault at the eastern boundary. (2) In central NCC, the Taihang Orogenic belt located in the central NCC is characterized by a segmented density anomaly distribution. (3) In Western NCC, the Qilian block in the western NCC presents a clockwise rotation of the density anomaly distribution with an increasing lithospheric depth, while the adjacent Ordos block remains continuously stable. (4) Across the Taihang Orogenic belt in the central NCC and the Qilian-Qaidam blocks in the western NCC, stronger impacts of the orogenic belt and a high heat flux environment are observed, which results in an upwelling of the deeply buried asthenospheric substances and, consequently, a reconstruction of the lithospheric density structure distribution.

1085

1090

1095

Code and data availability. The on-orbit GOCE gravity gradient data can be browsed and downloaded from GOCE+ Geoexplore II (<http://goce.kma.zcu.cz/data.php>). The software "Tesseroids" for gravity gradient topographic correction and interface undulation can be browsed and downloaded from <https://tesseroids.readthedocs.io/en/latest>. The global crustal model CRUST1.0 can be downloaded from <https://igppweb.ucsd.edu/~gabi/crust1.html>. The processed gravity gradient data and inversion results can be browsed and downloaded from <https://zenodo.org/record/3545809#.XdJ5H695vIU>.

1100

Author contributions. Conceptualization, YW; methodology, YT; validation, YT, writing original draft preparation, YT; writing review and editing, YT; supervision, YW; funding acquisition, YW.

Competing interests. The authors declare no conflict of interest.

1105

Acknowledgements. We are grateful to editor Prof. Mioara Mandea and two reviewers for providing a lot of constructive comments and suggestions, which really help us a lot to make remarkable progress. We are grateful to Prof. Xinsheng Wang in Development Research Center of China Earthquake Administration for providing corrected gravity data. We are also grateful to Prof. Qi Lin and Prof. Bojie Yan in Minjiang University for providing a lot of help when we prepared this paper.

1110

Financial support. This research was funded by the R&D of Key Instruments and Technologies for Deep Resources Prospecting (the National R&D Projects for Key Scientific Instruments), grant number No.ZDYZ2012-1-04.

1115

References

- Amante, C., and Eakins, B.W.: ETOPO1 1 arc-minute global relief model: Procedures, data sources and analysis, NOAA Technical Memorandum NESDIS NGDC-24, Boulder, Colorado, USA, March 2009, 19, 2009.
- 1120 An, M.J., and Shi, Y.L.: Three-dimensional thermal structure of the Chinese continental crust and upper mantle, *Sci. China Ser. D, Earth Sciences*, 50 (10), 1441-1451, doi:10.1007/s11430-007-0071-3, 2007.
- Bowin, C., Scheer, E., and Smith, W.: Depth estimates from ratios of gravity, geoid, and gravity gradient anomalies, *Geophysics*, 51 (1), 123-136, doi:10.1190/1.1442025, 1986.
- Capriotti, J., and Li, Y.: Gravity and gravity gradient data: Understanding their information content through joint inversions, 1125 *Proceedings of the 84th SEG Annual International Meeting, Denver, Colorado, USA, October 2014*, 1329-1333, 2014.
- Chen, L., Zheng, T. Y., and Xu, W. W.: A thinned lithospheric image of the Tanlu Fault Zone, eastern China: Constructed from Wave equation based receiver function migration, *J. Geophys. Res.: Sol. Ea.*, 111, B9, doi: 10.1029/2005JB003974, 2006.
- Constable, S.C., Parker, R.L., and Constable, C.G.: Occam's inversion: A practical algorithm for generating smooth models 1130 from electromagnetic sounding data, *Geophysics*, 52 (3), 289-300, doi:10.1190/1.1442303, 1987.
- Fang, J.: Three-dimensional density distribution of lithosphere in North China, *Geophys. Geochem. Explor.*, 23 (3), 179-184, 1996.
- Gao, S., Zhang, J.F., Xu, W.L., and Liu, Y.S.: Delamination and destruction of the North China Craton, *Chinese Sci. Bull.*, 54, 3367-3378, doi:10.1007/s11434-009-0395-9, 2009.

- 1135 Ge, C., Zheng, Y., and Xiong, X.: Study of crustal thickness and Poisson ratio of the North China Craton, *Chinese J. Geophys.*, 54 (10): 2538-2548, doi:10.3969/j.issn.0001-5733.2011.10.011, 2011.
- Hansen, P.C.: Analysis of discrete ill-posed problems by means of the L-curve, *Siam Rev.*, 34 (4), 561-580, doi:10.1137/1034115, 1992.
- Huang, J., and Zhao, D.: Seismic imaging of the crust and upper mantle under Beijing and surrounding regions, *Phys. Earth Planet. In.*, 173 (3-4), 330-348, doi:10.1016/j.pepi.2009.01.015, 2009.
- 1140 Laske, G., Masters, G., Ma, Z., and Pasyanos, M.: Update on CRUST1.0-a1-degree global model of Earth's crust, *Geophysical Research Abstracts*, 15, Abstract EGU2013-2658, doi:10.6092/1970-9870/128, 2013.
- Li, H., Shen, C., Sun, S., Wang, X., Xiang, A., and Liu, S.: Recent gravity changes in China Mainland, *Geodesy Geodyn.*, 2(1), 1-12, doi:10.3724/SP.J.1246.2011.00001, 2011.
- 1145 Li, H.L., Fang, J., Wang, X.S., Liu, J., Cui, R.H., and Chen, M.: Lithospheric 3-D density structure beneath the Tibetan plateau and adjacent areas derived from joint inversion of satellite gravity and gravity-gradient data, *Chinese J. Geophys.*, 60 (6), 2469-2479, doi:10.6038/cjg20170634, 2017.
- Li, Y., and Oldenburg, D.W.: 3-D inversion of magnetic data, *Geophysics*, 61 (2), 394-408, doi:10.1190/1.1443968, 1996.
- Li, Z., Hao, T., and Xu, Y.: Uppermost mantle structure of the North China Craton: Constraints from interstation Pn travel time difference tomography, *Chin. Sci. Bull.*, 56, 1691, doi:10.1007/s11434-011-4487-y, 2011.
- 1150 Liu, R., Wu, Z., Yin, C., Chen, Y., and Zhuang, C.: Development of China digital seismological observational systems, *Acta Seismol. Sinica*, 16(5), 568-573, doi:10.1007/BF02893477, 2003.
- Moritz, H.: Geodetic reference system 1980, *Bull. Geodesique*, 54, 395-405, doi: 10.1007/BF02521480, 1980.
- Martinec, Z.: Mass-density Green's functions for the gravitational gradient tensor at different heights, *Geophys. J. Int.*, 196 (3), 1455-1465, doi: 10.1093/gji/ggt495, 2014.
- 1155 Nagy, D., Papp, G., and Benedek, J.: The gravitational potential and its derivatives for the prism, *J. Geodesy*, 74, 552-560, doi: 10.1007/s001900000116, 2000.
- Pavlis, N.K., Holmes, S.A., Kenyon, S.C., and Factor, J.K. The development and evaluation of the Earth Gravitational Model 2008 (EGM2008), *J. Geophys. Res.: Sol. Ea.*, 117, B04406, doi:10.1029/2011JB008916, 2012.
- 1160 Pilkington, M.: 3-D magnetic imaging using conjugate gradients, *Geophysics*, 62 (4), 1132-1142, doi:10.1190/1.1444214, 1997.
- Pilkington, M.: 3D magnetic data-space inversion with sparseness constraints, *Geophysics*, 74 (1), L7-L15, doi:10.1190/1.3026538, 2009.
- Qin, P., Huang, D., Yuan, Y., Geng, M., and Liu, J.: Integrated gravity and gravity gradient 3D inversion using the non-linear conjugate gradient, *J. Appl. Geophys.*, 126, 52-73, doi:10.1016/j.jappgeo.2016.01.013, 2016.
- 1165 Rummel, R., Yi, W., and Stummer, C.: GOCE gravitational gradiometry, *J. Geodesy*, 85, 777-790, doi:10.1007/s00190-011-0500-0, 2011.

- Sebera, J., Šprlák, M., Novák, P., Bezděk, A., and Vařko, M.: Iterative spherical downward continuation applied to magnetic and gravitational data from satellite, *Surv. Geophys.*, 35 (4), 941-958, doi:10.1007/s10712-014-9285-z, 2014.
- 1170 Sheng, S. Z., Wan, Y. G., Huang, J. C., Bu, Y. F., Li, X.: Present tectonics stress field in the Circum-Ordos region deduced from composite focal mechanism method, *Chinese J. Geophys.*, 58 (2), 436-452, doi: 10.6038/cjg20150208, 2015.
- Šprlák, M.: A graphical user interface application for evaluation of the gravitational tensor components generated by a level ellipsoid of revolution, *Comput. Geosci.*, 46, 77-83, doi:10.1016/j.cageo.2012.04.013, 2012.
- 1175 Su, J., Zhu, W., Lu, H., Xu, M., Yang, W., and Zhang, Z.: Geometry styles and quantification of inversion structures in the Jiyang depression, Bohai Bay Basin, eastern China, *Mar. Petrol. Geol.*, 26 (1), 25-38, doi:10.1016/j.marpetgeo.2007.08.003, 2009.
- Szwillus, W., Ebbing, J., Holzrichter, N.: Importance of far-field topographic and isostatic corrections for regional density modelling, *Geophys. J. Int.*, 207(1), 274-287, doi:10.1093/gji/ggw270, 2016.
- 1180 Teng, J., Wang, F., Zhao, W., Zhang, Y., Zhang, X., Yan, Y., Zhao, J., Li, M., Yang, H., Zhang, H., and Ruan, X.: Velocity structure of layered block and deep dynamic process in the lithosphere beneath the Yinshan orogenic belt and Ordos Basin, *Chinese J. Geophys.*, 53 (1), 67-85, doi:10.3969/j.issn.0001-5733.2010.01.008, 2010.
- Teng, J., Zhang, Z., Zhang, B., Yang, D., Wan, Z., and Zhang, H.: Geophysical fields and background of exceptional structure for deep latent mantle plume in Bohai Sea, *Chinese J. Geophys.*, 40, 468-480, 1997.
- 1185 Tian, Y., Ke, X., and Wang, Y.: DenInv3D: A geophysical software for three-dimensional density inversion of gravity field data, *J. Geophys. Eng.*, 15 (2), 354-365, doi:10.1088/1742-2140/aa8caf, 2018.
- Tian, Y., Ke, X., and Wang, Y.: A folding calculation method based on the preconditioned conjugate gradient inversion algorithm of gravity gradient tensor, *Pure Appl. Geophys.*, 176 (1), 215-234, doi:10.1007/s00024-018-1965-z, 2019a.
- Tian, Y., Ke, X., and Wang, Y.: Inversion of three-dimensional density structure using airborne gradiometry data in Kauring
1190 test site, *Geomatics and Information Science of Wuhan University*, 44 (4), 501-509, doi: 10.13203/j.whugis20160503, 2019b.
- Tian, Y., and Wang, Y.: Inversion of the density structure of the lithosphere in the North China Craton from GOCE satellite gravity gradient data, *Earth Planets Space*, 70, 173, doi:10.1186/s40623-018-0942-1, 2018.
- Tian, Y., and Zhao, D.: Destruction mechanism of the North China Craton: Insight from P and S wave mantle tomography, *J. Asian Earth Sci.*, 42 (6), 1132-1145, doi:10.1016/j.jseaes.2011.06.010, 2011.
- 1195 Tian, Y., Zhao, D., Sun, R., and Teng, J.: Seismic imaging of the crust and upper mantle beneath the North China Craton, *Phys. Earth Planet. In.*, 172 (3-4), 169-182, doi:10.1016/j.pepi.2008.09.002, 2009.
- Uieda, L., Barbosa, V.C.F., and Braitenberg, C.: Tesseroids: Forward-modeling gravitational fields in spherical coordinates, *Geophysics*, 81 (5), 41-48, doi:10.1190/geo2015-0204.1, 2016.
- 1200 Wang, X.S., Fang, J., and Hsu, H.: Density structure of the lithosphere beneath North China Craton, *Chinese J. Geophys.*, 55(4), 1154-1160, doi:10.6038/j.issn.0001-5733.2012.04.011, 2012.

- Wang, X.S., Fang, J., and Hsu, H.: 3D density structure of lithosphere beneath northeastern margin of the Tibetan Plateau, *Chinese J. Geophys.*, 56 (11), 3770-3778, doi:10.6038/cjg20131118, 10.1016/j.tecto.2013.11.002, 2013.
- 1205 Wang, X., Fang, J., and Hsu, H.: Three-dimensional density structure of the lithosphere beneath the North China Craton and the mechanisms of its destruction, *Tectonophysics*, 610 (6), 150-158, doi:10.1016/j.tecto.2013.11.002, 2014.
- Wu, L., Ke, X., Hsu, H., Fang, J., Xiong, C., and Wang, Y.: Joint gravity and gravity gradient inversion for subsurface object detection, *IEEE Geosci. Remote S.*, 10(4), 865-869, doi:10.1109/LGRS.2012.2226427, 2013.
- Xiong, X., and Teng, J.W.: Study on crustal movement and deep process in eastern Qinghai-Xizang Plateau, *Chinese J. Geophys.*, 45, 507-515, doi:10.1002/cjg2.266, 2002.
- 1210 Xu, Y., Zeyen, H., Hao, T., Santosh, M., Li, Z., Huang, S., and Xing, J.: Lithospheric structure of the North China Craton: Integrated gravity, geoid and topography data, *Gondwana Res.*, 34, doi:10.1016/j.gr.2015.03.010, 315-323, 2016.
- Yang, S., Xiong, X., Zheng, Y., and Shan, B.: Upper-mantle temperature and lithospheric thickness of North China, *Chinese J. Geophys.*, 56 (11), 3855-3867, doi:10.6038/cjg20131127, 2013.
- 1215 Yi, W., Rummel, R., and Gruber, T.: Gravity field contribution analysis of GOCE gravitational gradient components, *Stud. Geophys. Geod.*, 57 (2), 174-202, doi:10.1007/s11200-011-1178-8, 2013.
- Zandt, G., and Ammon, C. J.: Continental crust composition constrained by measurements of crustal Poisson's ratio, *Nature*, 374 (6518), 152, doi:10.1038/374152a0, 1995.
- Zhang, H. Q., Huang, Q. H., Zhao, G. Z., Guo, Z., and Chen, Y. J.: Three-dimensional conductivity model of crust and uppermost mantle at the northern trans North China Orogen: Evidence for a mantle source of Datong volcanoes, *Earth Planet Sc. Lett.*, 453, 182–192, doi: 10.1016/j.epsl.2016.08.025, 2016.
- 1220 Zhang, Y., Teng, J., Wang, F., Zhao, W., Li, M., and Wang, Q.: Structure of the seismic wave property and lithology deduction of the upper crust beneath the Yinshan orogenic belt and the northern Ordos block, *Chinese J. Geophys.*, 54 (1), 87-97, doi: 10.3969/j.issn.0001-5733.2011.01.010, 2011.
- Zhdanov, M.S., Ellis, R., and Mukherjee, S.: Three-dimensional regularized focusing inversion of gravity gradient tensor component data, *Geophysics*, 69 (4), 925-937, doi:10.1190/1.1778236, 2004.
- 1225 Zhu, R.X., Yang, J.H., and Wu, F.Y.: Timing of destruction of the North China Craton, *Lithos*, 149 (15), 51-60, doi:10.1016/j.lithos.2012.05.013, 2012.
- Zhu, R. X.: Review of the achievements of major research plan on “Destruction of North China Craton” (in Chinese), *China Sci Foundation*, 32, 282–290.
- 1230